Author's personal copy

Ouaternary Science Reviews 62 (2013) 114-141



Contents lists available at SciVerse ScienceDirect

Quaternary Science Reviews

journal homepage: www.elsevier.com/locate/quascirev



The Last Glacial Maximum at 44°S documented by a ¹⁰Be moraine chronology at Lake Ohau, Southern Alps of New Zealand

Aaron E. Putnam ^{a,b,*}, Joerg M. Schaefer ^{a,c}, George H. Denton ^b, David J.A. Barrell ^d, Sean D. Birkel ^b, Bjørn G. Andersen ^{e,1}, Michael R. Kaplan ^a, Robert C. Finkel ^f, Roseanne Schwartz ^a, Alice M. Doughty ^g

- ^a Lamont-Doherty Earth Observatory, 61 Rt. 9W, Palisades, NY 10944, USA
- ^b Department of Earth Sciences, Climate Change Institute, University of Maine, Orono, ME 04469, USA
- ^c Department of Earth and Environmental Sciences, Columbia University, New York, NY 10027, USA
- ^d GNS Science, Private Bag 1930, Dunedin 9054, New Zealand
- ^e Department of Geosciences, University of Oslo, 0316 Oslo, Norway
- f Department of Earth and Planetary Sciences, University of California, Berkeley, CA 95064, USA
- g Antarctic Research Centre, School of Earth Sciences, Victoria University of Wellington, PO Box 600, Wellington, New Zealand

ARTICLE INFO

Article history: Received 17 March 2012 Received in revised form 24 October 2012 Accepted 29 October 2012 Available online

Keywords:
Last Glacial Maximum
Southern Ocean
Glacier
Geomorphology
¹⁰Be
Surface-exposure dating
Cosmogenic nuclide
Paleoclimatology
Southern Alps
New Zealand
Antarctica
Patagonia
Glaciology
Snowline
Last Glacial termination

ABSTRACT

Determining whether glaciers registered the classic Last Glacial Maximum (LGM; \sim 26,500— \sim 19,000 yrs ago) coevally between the hemispheres can help to discriminate among hypothesized drivers of ice-age climate. Here, we present a record of glacier behavior from the Southern Alps of New Zealand during the 'local LGM' (LLGM). We used 10 Be surface-exposure dating methods and detailed glacial geomorphologic mapping to produce a robust chronology of well-preserved terminal moraines deposited during the LLGM near Lake Ohau on central South Island. We then used a glaciological model to estimate a LLGM glacier snowline and atmospheric temperature from the Ohau glacier record.

Seventy-three 10 Be surface-exposure ages place culminations of terminal moraine construction, and hence completions of glacier advances to positions outboard of present-day Lake Ohau, at 138,600 \pm 10,600 yrs, 32,520 \pm 970 yrs ago, 27,400 \pm 1300 yrs ago, 22,510 \pm 660 yrs ago, and 18,220 \pm 500 yrs ago. Recessional moraines document glacier recession into the Lake Ohau trough by 17,690 \pm 350 yrs ago. Exposure of an ice-molded bedrock bench located inboard of the innermost LLGM moraines by 17,380 \pm 510 yrs ago indicates that the ice tongue had receded about 40% of its overall length by that time. Comparing our chronology with distances of retreat suggests that the Ohau glacier terminus receded at a mean net rate of about 77 m yr $^{-1}$ and its surface lowered by 200 m between 17,690 and 17,380 yrs ago. A long-term continuation of ice retreat in the Ohau glacier catchment is implied by moraine records at the head of Irishman Stream valley, a tributary of the Ohau glacier valley. The Irishman Stream cirque glacier advanced to produce a set of Lateglacial moraines at 13,000 \pm 500 yrs ago, implying that the cirque glacier was less extensive prior to that advance.

We employed a glaciological model, fit to these mapped and dated LLGM moraines, to derive snowline elevations and temperature parameters from the Ohau glacier record. The modeling experiments indicate that a snowline lowering of 920 \pm 50 m and temperature depression of 6.25 \pm 0.5 °C below modern values allows for the Ohau glacier to grow to an equilibrium position within the LGM moraine belt. Taken together with a glaciological simulation reported from the Irishman Stream valley, snowlines and temperatures increased by at least $\sim\!520$ m and $\sim\!3.6$ °C, respectively, between $\sim\!18,\!000$ and $\sim\!13,\!000$ yrs ago.

Climate parameters derived from the Ohau glacier reconstruction are similar to those derived from glacier records from Patagonia, to air temperature indicators from Antarctica, as well as to sea-surface temperature and stratification signatures of the Southern Ocean. We think that the best explanation for the observed southern LLGM is that southern winter duration modulated Southern Ocean sea ice, which in turn influenced Southern Ocean stratification and made the surface ocean cooler. Orbitally induced cooling of the Southern Ocean provides an explanation for the LLGM in the Southern Alps having

^{*} Corresponding author. Lamont-Doherty Earth Observatory, 61 Rt. 9W, Palisades, NY 10944, USA.

E-mail address: aputnam@ldeo.columbia.edu (A.E. Putnam).

¹ Deceased.

been coincident with the northern LGM. We argue further that the global effect of North Atlantic stadials led to disturbance of Southern Ocean stratification, southward shifts of the subtropical front, and retreat of Southern Alps glaciers. Collapse of Southern Ocean stratification during Heinrich Stadial-1, along with attendant sea-surface warming, triggered the onset of the Last Glacial termination in the Southern Alps of New Zealand.

© 2012 Elsevier Ltd. All rights reserved.

1. Introduction

Late Quaternary ice-age cycles have constituted the fundamental pulse beat of Earth's climate system over the past one million years, but a complete explanation of these cycles has yet to emerge. Variations of ice volume, dominated by Northern Hemisphere ice sheets, resemble orbital frequencies in general (Hays et al., 1976) and the summer insolation intensity signal at 65°N in particular (Broecker, 1966; Broecker and van Donk, 1970), as was predicted by Milankovitch (1941). Additional support for Milankovitch (1941) comes from the close match between the rate of change of global ice volume and June insolation at 65°N (Roe, 2006). In particular, Northern Hemisphere ice sheets most recently attained maximum sizes during a prominent trough in the boreal summer insolation intensity curve at 26,500-19,000 yrs ago, known classically as 'the Last Glacial Maximum' (LGM; Mix et al., 2001; Clark and Mix, 2002; Clark et al., 2009; MARGO Project Members, 2009). But there are problems with regard to the Southern Hemisphere. For example, Hays et al. (1976) showed that, over the last 300,000 yrs, biological indicators of Southern Ocean sea-surface temperature (SST) and water-column stratification fluctuated in phase with northern ice sheets, despite different signatures of precession-dominated insolation in each hemisphere. Moreover, Mercer (1984) identified simultaneous glacier expansion during the classic LGM in both southern and northern middle-to-high latitudes. Because summer insolation intensity is out-of-phase during the LGM at those latitudes, the apparent north-south synchrony presents a conundrum that Mercer (1984) called "a fly in the ointment of Milankovitch Theory" (p. 307). The solution to this problem requires an explanation for full-glacial climatic conditions in the Southern Hemisphere during the classic LGM.

To address this issue, we start by documenting the initiation, duration, magnitude, and termination of the Local Last Glacial Maximum (LLGM) cold period in the Southern Alps of New Zealand. We focused on the geomorphology and chronology of an exceptionally well-preserved set of moraines deposited by an ice-age glacier, referred to here as the Ohau glacier, which occupied the Lake Ohau valley on the eastern side of the Southern Alps. This moraine chronology utilizes recent analytical improvements in ¹⁰Be surface-exposure dating (e.g., Schaefer et al., 2009), as well as a local ¹⁰Be production-rate calibration site (Putnam et al., 2010b). Glaciers in the Southern Alps are regarded as sensitive recorders of atmospheric temperatures (e.g., Oerlemans, 1997; Anderson and Mackintosh, 2006; Anderson et al., 2010; Purdie et al., 2011). We then employ a version of the University of Maine Ice Sheet glaciological model (UMISM) adapted to mountain-glacier reconstruction to estimate the temperature conditions, relative to modern values, required to generate ice of LLGM extent in the Ohau valley. Using the moraine chronology and glacier-climate reconstruction, we assess potential drivers of Southern Hemisphere ice-age climate. In this regard, the Southern Alps are well positioned for evaluating hypothesized mechanisms of global climate change because they are at the antipode of the North Atlantic region, far distant from northern ice sheets as well as from sites of North Atlantic Deep Water formation.

2. Setting

South Island, New Zealand (40–46°S, 164–170°W) is situated just north of the modern position of the subtropical front (STF) in the South Pacific Ocean, in the southern westerly wind belt (Fig. 1). Produced by oblique convergence of the Indo-Australian and Pacific plates, the Southern Alps form the spine of South Island and reach altitudes in excess of 2000 m on the main drainage divide (hereafter "Main Divide"). Heavily faulted, uplifted Mesozoic sedimentary rocks constitute the central Southern Alps east of the Main Divide. Highly indurated quartzofeldspathic greywacke sandstones and argillite mudstones are among the most common lithologies (Cox and Barrell, 2007).

The Southern Alps impose a strong föhn effect on the prevailing westerly winds, inducing 10 m yr⁻¹ or more precipitation (water equivalent) just northwest of the Main Divide. Precipitation declines with increasing distance southeast of the Main Divide (Henderson and Thompson, 1999). More than 3000 inventoried glaciers cover 1158 km² of the Southern Alps (Chinn et al., 2005). The present-day snowline is ~1500 m above sea level (a.s.l.) just west of the Main Divide at Franz Josef Glacier, and trends upwards to >2200 m a.s.l. east of the Main Divide at the Ben Ohau Range (Lamont et al., 1999). High precipitation totals in ice catchment basins of the central Southern Alps result in large ice fluxes through outward-flowing glaciers. Such rapid ice throughput elevates glacier sensitivity to atmospheric temperature variations, resulting in response times to climate change of decades or less for many glaciers of the Southern Alps (e.g., Anderson et al., 2010). Historical records of variations of glacier lengths show that non-calving glacier termini have fluctuated in-step during the last century on both flanks of the Southern Alps. Thus, glaciers on opposite sides of the Main Divide register a common climate signal on decadal-to-centurial timescales (Chinn, 1996; Burrows, 2005; Barrell et al., 2011).

In foreland regions, moraine belts outline former ice tongues that flowed outward from the Southern Alps during recent glaciations (Suggate, 1990; Barrell, 2011; Barrell et al., 2011), and associated glaciofluvial outwash plains extend coastwards. Northwest of the Main Divide, post-glacial coastal erosion has truncated some distal parts of the LLGM moraine belts in some valleys. However, well-preserved moraine systems rim the LLGM glacial troughs that contain Lake Tekapo, Lake Pukaki, and Lake Ohau at the western margin of the Mackenzie basin southeast of the highest sector of the Southern Alps. The glaciers that occupied these troughs deposited numerous lateral and terminal moraine ridges during and following retreat from the LLGM. Moraines formed subsequently during Lateglacial time lie farther toward the heads of mountain valleys (Kaplan et al., 2010; Putnam et al., 2010a). These post LLGM landforms provide a basis for assessing glacier and climate changes during the Last Glacial termination.

3. Geomorphology

3.1. Overview of the Lake Ohau study area

The Ohau glacier tongue was produced by the coalescence of major tributary glaciers from the Hopkins River and Dobson River

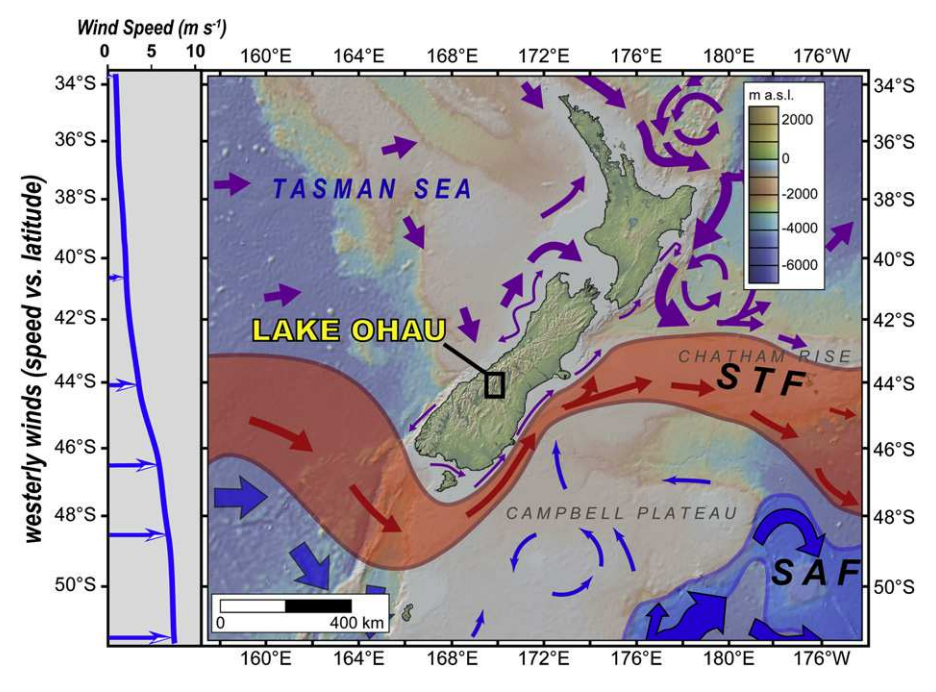


Fig. 1. Right panel: New Zealand with schematic depiction of surrounding physical oceanography (adapted from Carter et al., 1998). Arrows indicate surface-ocean currents, with purple denoting subtropical currents, red representing flow along the Subtropical Front (STF), and blue illustrating currents associated with the northern boundary of the Antarctic Circumpolar Current and the Subantarctic Front (SAF). Elevation color scale is inset. Left panel: Wind speed just west of New Zealand plotted versus latitude [derived from ECMWF ERA-Interim reanalysis data; averaged over the period AD1979 to AD2011 (Dee et al., 2011)]. (For interpretation of the references to color in this figure legend, the reader is referred to the web version of this article.)

valleys, both of which drain from the Main Divide. The overall catchment for this system at the LLGM was ~900 km². The Ohau glacial geomorphological assemblage is shown in Fig. 2 and is illustrated in Fig. 3. Farthest outboard are remnants of moraines and outwash older than the LLGM, while the LLGM moraine belts are more continuous and lie closer to the glacier trough. The assemblage of moraines and outwash surfaces has been influenced by the effects of uplift on the northwest side of the tectonically active Ostler Fault (Fig. 2) (Cox and Barrell, 2007). Outwash plains spilled through four gaps across the Ostler Fault uplift zone (Amos et al., 2007; Ghisetti et al., 2007). The Quailburn, Willowbank, Clearburn, and Ohau River gaps are former glacier meltwater spillways, with post-glacial drainage from Lake Ohau confined to the modern Ohau River (Fig. 2). Time-transgressive eastward meltwater deflection controlled by uplift along the Ostler Fault was instrumental in preserving outer terminal moraine belts (Amos

We divide glacial landforms near Lake Ohau into two groups on the basis of morphology and soil development (Cox and Barrell, 2007; Barrell et al., 2011); these groups have been attributed to the last two major glacial—interglacial cycles (Amos et al., 2007, 2010; Cox and Barrell, 2007; Barrell et al., 2011). Detailed geomorphological interpretations are shown in Fig. 2. Our glacial geomorphology mapping distinguishes topographic ridges of moraine from all other hummocky or irregular morainal landforms. In accord with the approach of Sugden and John (1976), we interpret an individual moraine ridge as marking a former position of the glacier margin, representing either a stillstand or a culmination of an advance of the ice margin. The material forming the crest of a moraine ridge was deposited immediately prior to withdrawal of the ice margin from that ridge.

Lake Ohau stands at 520 m above sea level (a.s.l.), and the Ohau moraine complex rises to as much as $\sim\!700$ m a.s.l. Pollen records from a site at similar altitude 20 km northeast of Lake Ohau (McGlone and Moar, 1998) indicates an early Holocene forest cover

of shrub and small-tree species, but that from mid-Holocene onwards, natural fire events led to a more open shrubland and grassland. Nothofagus forest spread into at least some parts of the area in the late Holocene. During the past ~800 years since human arrival, fire markedly reduced the native forest cover, resulting in widespread grassland (McGlone and Moar, 1998). Since European settlement ~150 years ago, frequent burning to assist pastoral farming has produced the modern vegetation of various introduced grasses, native short tussock (Festuca novae-zelandiae) and scattered patches of native and introduced shrubs. Introduced mammals, particularly rabbits and sheep, have generated small areas of soil erosion on the landforms. In recent years, a move away from burning practices has resulted in numerous wild-spreading patches of introduced pines and, on bouldery moraine ridges near Lake Ohau, considerable recolonization by native shrubs and tussocks. Patches of native forest persist in some tributaries of Lake Ohau, giving way to subalpine shrub and grassland above the local natural treeline at \sim 1200 m a.s.l.

3.2. Ohau I landforms

The outermost and hence oldest glacial landform assemblage (Ohau I) lies south and southeast of Lake Ohau and is mapped in green and olive in Fig. 2. The Ohau I landscape is gentle and rolling. Individual moraine ridges are typically $\sim\!2-5$ m high. Channeled outwash surfaces have a generally subdued form with patches of loess draped on sheltered surfaces. Boulders are few, and they commonly have shattered surfaces with spalled material accumulated around their bases.

The southeast sector of this landform assemblage is preserved at Table Hill, which has been uplifted, and tilted back to the northwest, by movement on the Ostler Fault (Amos et al., 2007; Ghisetti et al., 2007) (Figs. 2 and 4). At the crest of the Ostler Fault scarp, which forms the southeastern edge of Table Hill, vertical offset of the Ohau I landform assemblage is at least ~180 m, based on the

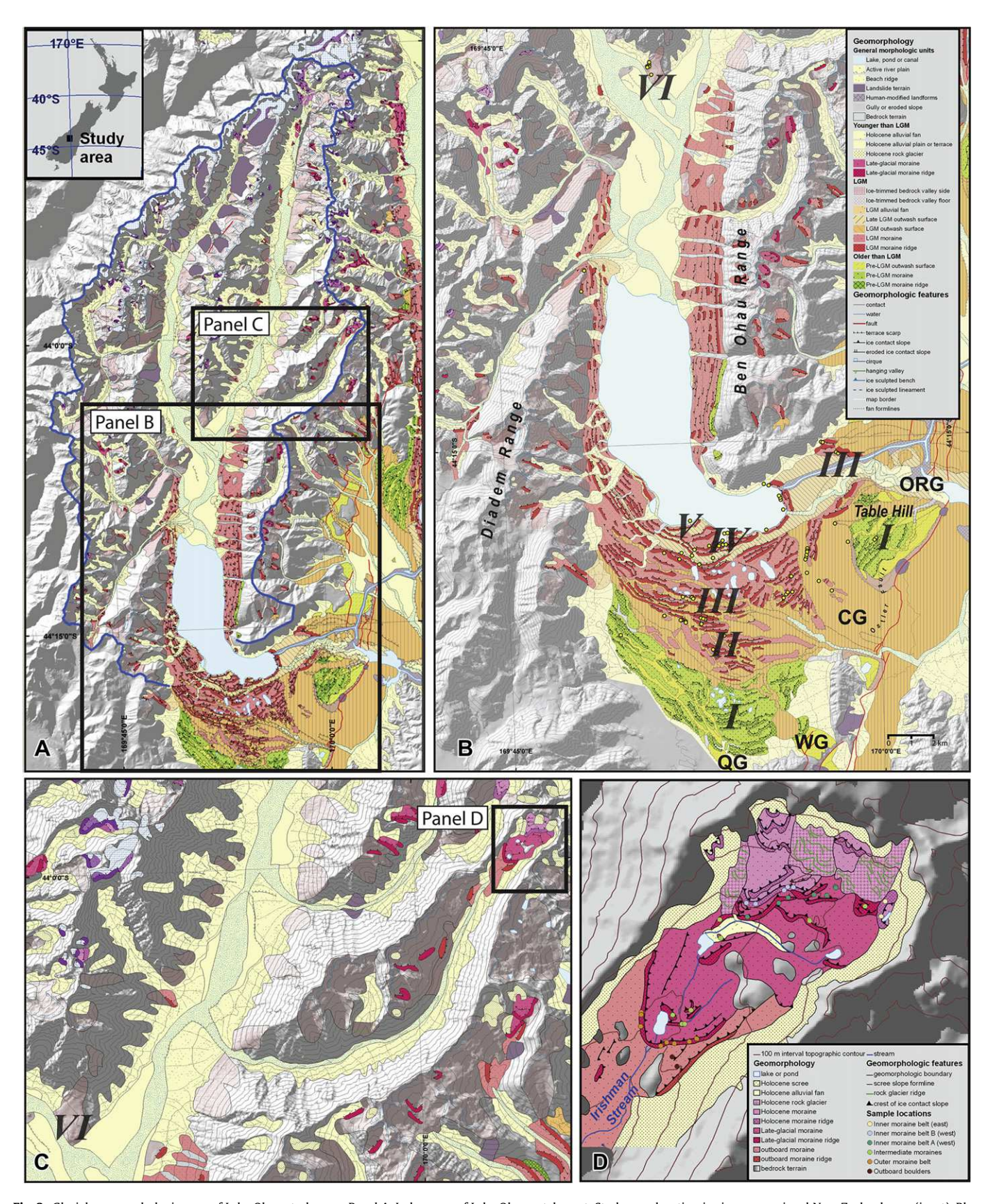


Fig. 2. Glacial geomorphologic map of Lake Ohau study area. Panel A. Index map of Lake Ohau catchment. Study area location is given on regional New Zealand map (inset). Blue line delineates catchment. Panel B. Detailed geomorphologic map of the Lake Ohau valley and foreland area. Roman numerals correspond to glacial geomorphologic landform assemblages described in text. ORG: Ohau River gap. CG: Clearburn gap. WG: Willowbank gap. QG: Quailburn gap. Yellow dots are locations of boulders sampled for ¹⁰Be surface-exposure dating. Geomorphologic legend is inset. Panel C. Map of Irishman Stream valley tributary of the Lake Ohau catchment. Panel D. Detailed geomorphologic map of glacier landforms at the head of Irishman Stream, adapted from Kaplan et al. (2010). Geomorphologic legend is inset. (For interpretation of the references to color in this figure legend, the reader is referred to the web version of this article.)



Fig. 3. Panorama of the Ohau terminal moraine complex. View is to the north. Terminal moraine ridges, ice-contact outwash plains, relict braided stream channels, and kettle lakes occupy the foreground. Lake Ohau is at center distance, with the Hopkins (left) and Dobson (right) river valleys in the center far distance. Ben Ohau Range is in the middle distance right of center, and Ohau Range is in distance on the left.

height of the scarp and the observation that Ohau II—III outwash lies, and presumably buries Ohau I deposits, on the downthrown side of the fault. The Table Hill glaciogenic deposits have been mapped in two regional formations; Balmoral Formation and, for older deposits on the crest of the fault scarp, Wolds Formation, by Gair (1967), Cox and Barrell (2007) and Amos et al. (2007).

The southern sector of the Ohau I landform assemblage comprises subdued moraines and outwash deposits north and west of Quailburn and Willowbank gaps. The trends of braided stream channels preserved on the outwash deposits indicate that meltwater flowed through the Willowbank and Quailburn gaps during construction of the Ohau I moraines.

3.3. Ohau II landforms

The moraines and outwash surfaces constituting the Ohau II landform assemblage (Figs. 2 and 5), situated inboard of Ohau I landforms, have a surface form that is distinctively sharper than the Ohau I landforms. For the most part, the Ohau II landforms are

patchy remnants, mainly of moraine and moraine ridges, preserved as islands surrounded by extensive Ohau III outwash plains (Figs. 2, 3, and 6). Moraine ridges in the southern portion of the Ohau II landform complex are broad and discontinuous. They stand 2–5 m high above neighboring general moraine or outwash surfaces. In contrast, the outer moraine ridges in the southwestern portion of the Ohau II landform complex are relatively sharp and continuous, with ridges typically 5–10 m high. The landforms mostly have stony surfaces, with rounded gravel common on general moraine. Scattered on the landforms are greywacke and semischist boulders (i.e., textural zones I and IIA/IIB, based on the classification used by Cox and Barrell, 2007).

The Ohau II glaciogenic deposits, along with those of Ohau III, are correlated with the regional Mt. John Formation (Gair, 1967; Amos et al., 2007; Cox and Barrell, 2007). The sharp-crested outer moraine ridges in the southwestern portion of the moraine complex are associated with aggradational outwash deposits, implying that these moraines were formed at the culmination of ice-margin advances (see Fig. 2). Relatively subdued inboard



Fig. 4. Table Hill and Ohau I moraine and outwash complex. View is to east, with Ostler Fault scarp, partly in shadow, delimiting the right (southeast) margin of Table Hill, with several landslides on the scarp face, and arrays of sinuous slump scars along the scarp crest. Ohau I moraine ridges trend from bottom to top of image on the northwesterly backtilted Table Hill platform. Fluvially eroded slopes define western and northern limits of Ohau I complex in center foreground and center distance, respectively. Ohau River, the Ohau and Pukaki hydro-electric canals, and Lake Ruataniwha (artificially dammed) are visible in distance.

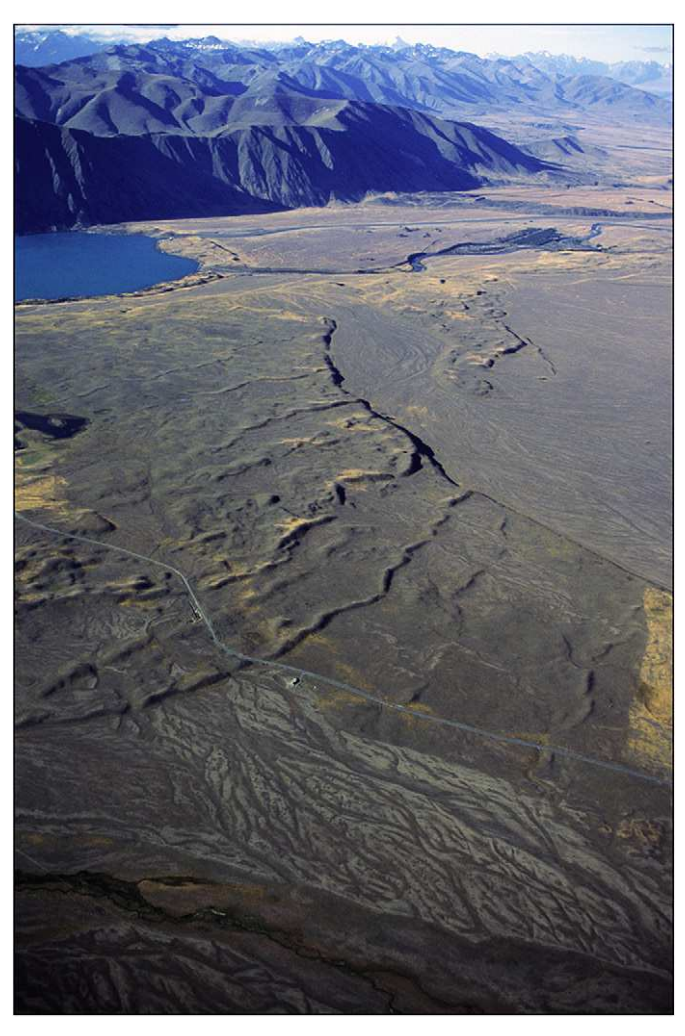


Fig. 5. Photograph of Ohau II (foreground, center-left), Ohau III (middle ground), and Ohau IV (left-distance) terminal moraine ridges. View is north. Prominent Ohau III ice-contact outwash plains with well-preserved relict braided stream channels are visible at bottom and middle of photograph. Aoraki/Mount Cook is tallest glaciated peak in far

topography, which includes moraine ridges in the southern sector of the Ohau II belt, suggests deposition during recession of the Ohau glacier terminus.

3.4. Ohau III landforms

Situated inboard of, and locally truncating, the Ohau II landforms is the Ohau III geomorphologic assemblage. The Ohau III glaciogenic deposits are correlated with the regional Mount John Formation (Gair, 1967; Amos et al., 2007; Cox and Barrell, 2007). The Ohau III moraine complex rims the southern perimeter of the Ohau glacier trough, from the eastern foot of the Ohau Range to the southern base of the Ben Ohau Range (Figs. 2 and 5). There are three main elements of the Ohau III complex. Sets of prominent, sharpcrested moraine ridges form the outer part of the complex. These ridges, standing as much as ~ 10 m above the adjacent ground, are among the tallest and most continuous moraine ridges observed in the entire study area. A central zone of the Ohau III moraine belt comprises rather featureless undulating ground moraine topography with numerous shallow lakes or depressions and relatively few moraine ridges; on the innermost side of Ohau III is a prominent, eroded ice-contact slope. Well-developed outwash plains

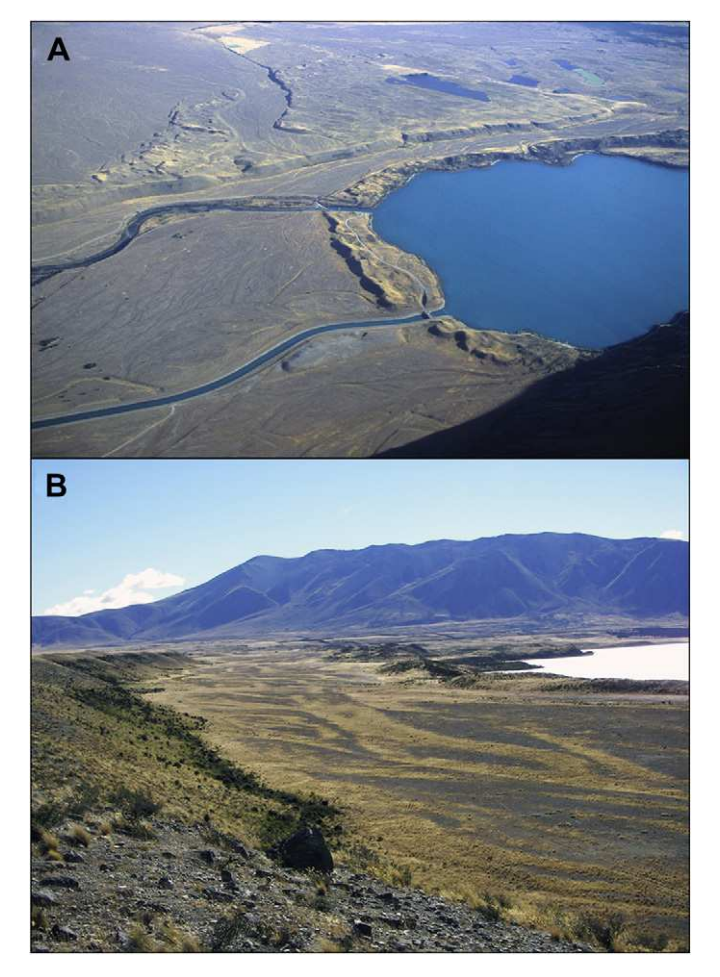


Fig. 6. Panel A. Oblique aerial photograph with view southwest toward Ohau IV moraine ridges and associated outwash (foreground), as well as Ohau III moraine ridges and associated outwash (distance, beyond prominent eroded ice-contact slope at far margin of Ohau IV outwash plain). Ohau Canal (lower) and Ohau River (center) drain left from the lake. Panel B. Photograph of Ohau IV outwash plain (middle). Vantage is west. Prominent Ohau IV terminal moraine ridge is in distance, and sharply defined eroded-ice-contact slope of innermost Ohau III is in immediate foreground. Ohau Range defines skyline. Note exceptionally well-preserved relict braided stream channels on Ohau IV outwash surface.

emanating from the Ohau III moraine belt extend through the Clearburn gap and the Ohau River gap (Figs. 2 and 5).

The Ostler Fault has produced a \sim 20 m vertical offset of Ohau III outwash surface at both gaps (Amos et al., 2007, 2010). The fault is interpreted to be a northwest-dipping listric thrust, on account of a substantial backtilt of the outwash surfaces, localized within \sim 2.5 km northwest of the fault scarp. This tilt pattern implies a rapid northwestward diminution of the tectonic uplift (Davis et al., 2005; Amos et al., 2007; Ghisetti et al., 2007). As a result, vertical movement associated with the Ostler Fault is highly localized along the hanging wall, and uplift at the Ohau II–V moraine belts is negligible (e.g., <1 mm yr $^{-1}$) in regard to surface-exposure dating calculations.

The middle to inner parts of the Ohau III moraine belt south of Lake Ohau exhibit a combination of generally featureless undulating topography, scattered discontinuous moraine ridges $\sim 1-5$ m high, numerous shallow lakes and an absence of abutting outwash deposits. This landscape formed during general recession of the Ohau glacier terminus.

The innermost Ohau III eroded ice-contact slope extends laterally for ~ 13 km, stands ~ 30 m above the Ohau IV outwash surface (Fig. 6), and approximates the outer margin of the trough into

which the Ohau glacier withdrew, following formation of the Ohau III moraine/outwash complex. This ice-contact slope could also represent an ice-margin advance or stillstand.

3.5. Ohau IV landforms

The Ohau IV moraine belt, dominated by prominent, sharp-crested ridges, forms a rim alongside the southern and eastern shores of the lake (Figs. 2 and 6). The associated outwash plain has been incised ~20–30 m by the modern Ohau River (Fig. 6). Many sub-rounded to sub-angular greywacke boulders, some exceeding 4 m in height, are embedded in or rest on the moraine ridges, as well as on the ice-contact heads of Ohau IV meltwater channels and outwash surfaces. The Ohau IV glaciogenic deposits, along with those of Ohau V and VI, are correlated with the regional Tekapo Formation (Gair, 1967; Amos et al., 2007; Cox and Barrell, 2007).

3.6. Ohau V landforms

The innermost features of the Lake Ohau terminal moraine complex are subdued discontinuous ridges along the southern shoreline of Lake Ohau that, at their northeastern ends, project into the Lake Ohau basin (Fig. 2). Two arcuate moraine ridges projecting northeastward into the lake mark the last positions occupied by the Ohau glacier before it withdrew into what is now the lake basin. Geomorphologic relationships indicate that these moraines were constructed at the edge of newly formed Lake Ohau (Fig. 2).

3.7. Ohau VI landforms

Glaciogenic landforms representing ice retreat from the Ohau V terminal positions are designated here as Ohau VI. These landforms include well-expressed lateral recessional moraines on the western side of the Ohau valley near the head of the lake, but

discrete landforms are more difficult to delineate on the eastern side of the valley, where broad ice-marginal benches span a large altitudinal range. The upper part of this flight of benches may reflect recession from older parts of the Ohau glacial landform sequence (e.g., Ohau III).

Included within the Ohau VI landform assemblage is an ice-molded bedrock bench at the junction of the Hopkins and Dobson rivers ~24 km north of the Ohau V terminal moraines (Figs. 2 and 7). A patchy veneer of lodgement till and scattered large greywacke boulders rest on the molded bedrock. This bedrock bench was exposed as the Ohau glacier receded from the southern end of the lake toward the head of the Lake Ohau catchment.

3.8. Irishman Stream moraines

At the LLGM, glacier ice from the Irishman Stream tributary valley merged with the Ohau glacier. Following substantial ice recession, glacier ice readvanced, producing prominent bouldery moraines within the cirque at the head of the Irishman Stream valley (Fig. 8). These moraines have been documented in detail by Kaplan et al. (2010), and are the youngest glacial geomorphologic features considered in this study.

3.9. Summary of geomorphological interpretations

We interpret the following sequence of events from the Lake Ohau glacial geomorphology. The Ohau glacier achieved its greatest recognized extent prior to the LLGM, as documented by the Ohau I landform assemblage. Incomplete preservation of the Ohau I moraine belt, exacerbated by uplift and tilting due to the Ostler Fault, reduces the certainty with which the ice extent and local paleogeography can be inferred. After uplift and tilting of the Ohau I landforms, the Ohau glacier expanded to construct the outboard Ohau II landforms, followed by ice retreat that produced the



Fig. 7. Oblique aerial photograph of ice-molded landforms near the junction of the Hopkins (background) and Dobson (behind the photographer) rivers. Vantage is west. These bedrock landforms comprise part of the Ohau VI landform assemblage. Note broad ice-scour troughs and ridges aligned right to left on the crest of the bench, parallel to the Hopkins valley ice-flow direction, and a dark line in the foreground at the edge of the bench crest, marking a low (~1 m high) Dobson valley recessional lateral moraine. Barrier Range defines the skyline.

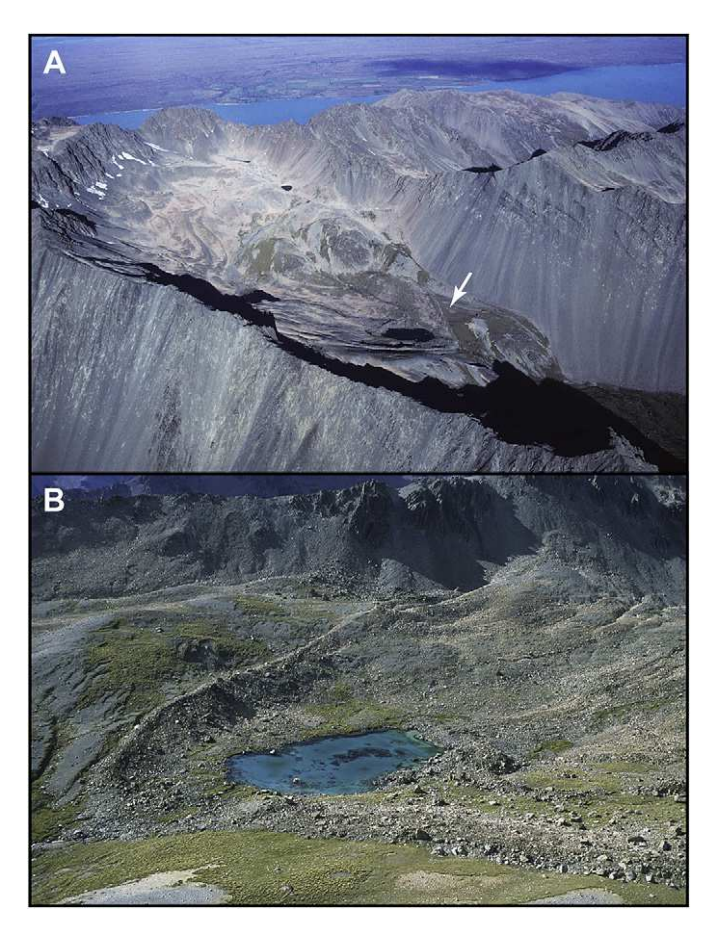


Fig. 8. Irishman Stream moraine set. A.) Overview photograph of glacier landforms at the head of Irishman Stream valley. Vantage is east. B.) Photograph of outer prominent bouldery moraine ridge at head of Irishman Stream valley. Vantage is west (depicted by arrow in Panel A).

inboard Ohau II recessional moraines. A subsequent ice advance, which in places overran parts of the Ohau II moraine belt, culminated with formation of the near-continuous outer Ohau III moraine ridges. The inner ~3 km of the central portion of Ohau III moraine belt comprises subdued and discontinuous moraines formed during recession from the Ohau III maximum. The eroded ice-contact slope that forms the inner margin of the Ohau III moraine belt is thought to mark the edge of the glacier trough as it existed at Ohau III time. Alternatively, this ice-contact slope may represent an ice-margin advance or stillstand position. The Ohau IV moraines were formed at the culmination of a subsequent resurgence of the glacier, by which time meltwater outflow had become confined to the Ohau River gap. Moraine ridges of the inboard Ohau V moraine belt mark brief pauses in recession from the Ohau IV ice limit. Subsequent terminus retreat and ice-surface lowering exposed the bedrock bench near the Hopkins/Dobson junction that comprises part of the Ohau VI landform assemblage. Recession continued well into mountain valleys, after which time a glacier at the head of Irishman Stream tributary valley (and probably other glaciers in the Ohau catchment headwaters) readvanced to produce Lateglacial moraines (Kaplan et al., 2010).

4. Methods

4.1. Sample collection

We sampled only boulders on landforms with clear geomorphologic context relating directly to a former glacier margin (Fig. 9). Integrated with the geomorphologic mapping study, we targeted specific moraine crests for sampling based on the following criteria: (1) crests represent single, distinguishable ice-marginal positions; (2) moraines do not appear to have been reworked by post-depositional processes, including human influence; and (3) landforms are clearly defined and retain pristine features such as perched erratics and abandoned ice-marginal outwash fans with preserved braided stream channels (e.g., Fig. 6), all indicating little landform change since initial formation.

Where possible, we sampled several boulders on each moraine ridge. Boulders were selected based on the following considerations:

- (1) Geomorphologic integrity. We assessed the immediate surroundings of each sampled boulder to ensure there were no indications of post-depositional disturbance by slope processes, fluvial reworking, or human activities. Ideal boulders are those rooted in moraine ridge crests, and they occur away from steep slopes of landforms that may have experienced degradation as well as adjacent hill slopes that may have shed rock-fall debris onto the moraine area. We generally did not sample boulders with heights less than 50 cm above ground level.
- (2) Boulder surface integrity. We avoided sampling boulders that are heavily jointed, fractured, pitted, and/or exhibit evidence of spalling or granular disintegration. Preference was given to sampling from the top center of boulders with near-horizontal, planar, or gently rounded upper surfaces, keeping away from any steep edges at the boulder sides.

Boulder surfaces were sampled using hammer and chisel or the 'drill-and-blast' method of Kelly (2003). We used clinometer and compass to document the surrounding topographic shielding for all sample locations. We photographed all boulders from several different perspectives, and we measured the ground-to-sample height on four sides of every boulder.

4.2. ¹⁰Be extraction and AMS measurements

Samples were processed for ¹⁰Be analysis at the Lamont-Doherty Earth Observatory (LDEO) Cosmogenic Isotope Laboratory using the methods of Schaefer et al. (2009). The LDEO procedure is available online at: http://www.ldeo.columbia.edu/tcn. Beryllium ratios (¹⁰Be/⁹Be) were measured with the CAMS accelerator at the Lawrence-Livermore National Laboratory. Samples processed before September 2007 were measured relative to the KNSTD standard (${}^{10}\text{Be}/{}^{9}\text{Be} = 3.15\text{e}^{-12}$). Samples processed during and after September 2007 were measured relative to the 07KNSTD standard $[^{10}Be]^9Be = 2.85e^{-12}$; based on a revised ^{10}Be half-life of 1.36 ± 0.07 Ma (Nishiizumi et al., 2007)]. After measurement, ¹⁰Be/⁹Be ratios were corrected for residual boron contamination and ${}^{10}\mathrm{Be}$ in procedural blanks. All blank corrections were less than 1.5%. All samples measured relative to the KNSTD standard were subsequently normalized to 07KNSTD by applying a correction factor of 0.9042 (Nishiizumi et al., 2007).

4.3. Exposure-age calculations

We calculated surface-exposure ages using the sea-level high-latitude (SLHL) ¹⁰Be production rates of Putnam et al. (2010b) and scaling methods of Stone (2000; 'St'), Desilets et al. (2006; 'De'), Dunai (2001; 'Du'), and Lifton et al. (2005, 2008; 'Li'), as well as a version of the Stone (2000) scaling that incorporates a high-resolution version of the Lifton et al. (2008) geomagnetic model (Putnam et al., 2010b), labeled 'Lm'. Abbreviations follow the

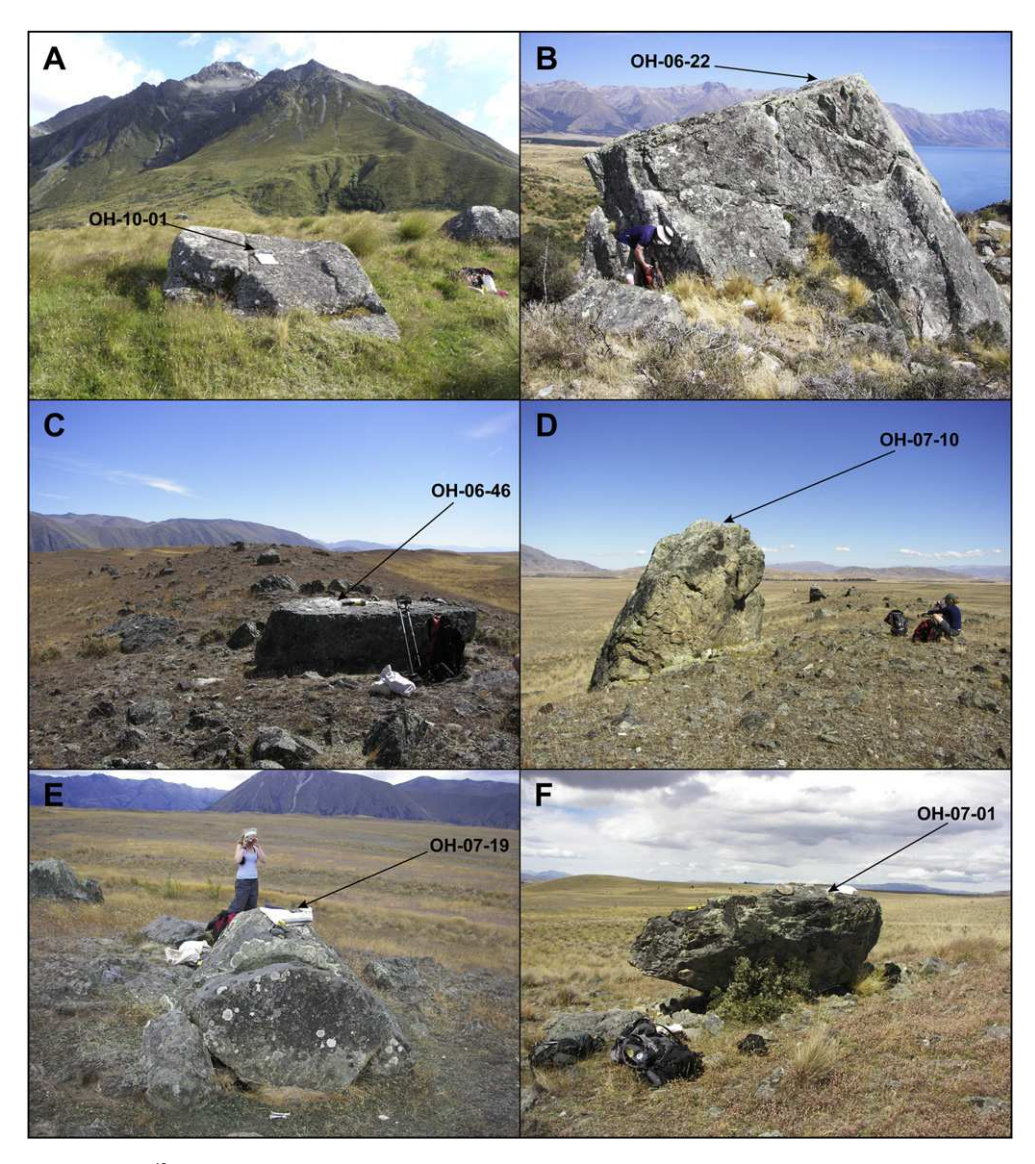


Fig. 9. Examples of boulders sampled for ¹⁰Be surface-exposure dating. Panel A. Photograph, with vantage north, of boulder embedded in Ohau VI ground moraine overlying ice-molded bedrock. Panel B. Photograph, vantage northwest, of large boulder embedded in top of outermost Ohau IV moraine ridge ice-contact slope. Panel C. Photograph, vantage west, of boulder resting on top of outermost Ohau III moraine ridge crest. Panel D. Photograph, vantage west-southwest, of large boulder embedded in ice-distal slope of outermost Ohau III moraine ridge. Panel E. Photograph, vantage north, of boulder resting on subdued Ohau II moraine ridge remnant that is surrounded by Ohau III outwash. Panel F. Photograph, vantage east, of boulder resting on Ohau II moraine ridge.

nomenclature of Balco et al. (2008). Tectonic and glacioisostatic uplift rates at the Lake Ohau moraines are assumed to be negligible (Putnam et al., 2010b) for moraines away from the Ostler Fault (i.e., all moraines except for Ohau I). Even for the Ohau I moraine, a landscape uplift rate of 1 mm yr $^{-1}$ (the proposed localized uplift rate on the northwest side of the Ostler Fault scarp adjacent to the study area; Amos et al., 2010) would decrease ages by less than 1% (i.e., within the analytical uncertainty of the data, reported below). Accordingly, we did not apply a correction for the effects of landscape uplift to any of the landforms dated in this study.

Changes in local atmospheric pressures at sea level during the last ice age (i.e., since boulder deposition) could have resulted in slightly higher production rates due to equatorward-shifted westerlies and hence lower atmospheric pressures in southern middle latitudes (e.g., Staiger et al., 2007). In this regard, a ^{14}C -dated LLGM-age production-rate test site reported by Putnam et al. (2010b) verified the suitability of an early-Holocene production-rate calibration data set for calculating the age of an \sim 18,000-yr surface, indicating that

temporal shifts in average air pressure, if any, have not had any discernible influence on ¹⁰Be production since the end of the LLGM. This finding is consistent with the modeling results of Staiger et al. (2007) for the atmosphere over New Zealand. For these reasons we did not apply a correction for changes in atmospheric pressure.

An erosion rate was not incorporated into age calculations due to the resistant nature of the greywacke boulder surfaces (Birkeland, 1982; Schaefer et al., 2006, 2009). Furthermore, as no erosion correction was applied to the production-rate calibration data set of Putnam et al. (2010b), any common effects of erosion on this rock type have already been integrated into the SLHL ^{10}Be production rate. We followed Schaefer et al. (2006, 2009) and Putnam et al. (2010b) and did not apply a snow-cover correction for the following reasons: (1) snowfalls are infrequent at elevations below ~ 1500 m a.s.l. in the Southern Alps, (2) at lower elevations, winter snow rarely exceeds depths of ~ 1 m and tends to melt away within days to weeks, and (3) salient boulder tops and moraine ridge crests are generally windswept and free of snow throughout the winter.

4.4. Glaciological modeling

We constrained a glaciological model to mapped and dated moraines (Fig. 2) in order to estimate likely LLGM climatic parameters and average equilibrium-line altitude (hereafter, snowline) for the Ohau glacier. This aspect of work was carried out using the University of Maine Ice Sheet Model (UMISM), a 2D finite-element mass and momentum ice dynamics solver with embedded components for calculating isostasy, thermodynamics, sliding, and surface mass balance (Fastook and Prentice, 1994; Fastook et al., 2008) (see Appendix). The force balance in UMISM follows the Shallow Ice Approximation (SIA) (vertically integrated momentum combined with continuity) where the dominant stress is internal shear, and where longitudinal stresses are neglected. Although models of this sort are most commonly used for simulating ice sheets, they are also applicable in mountain settings for large trunk glaciers flowing over gently sloping beds (Le Meur and Vincent, 2003; Le Meur et al., 2004, 2007; Leysinger Vieli and Gudmundsson, 2004; Schäfer et al., 2008). Other SIA modeling studies over domains comparable in scale to the Ohau valley include the Wasatch (Laabs et al., 2006) and Uinta (Refsnider et al., 2008) mountains, Utah, USA, and the Wind River Range, Wyoming, USA (Birkel et al., 2012).

Primary input to UMISM was a 500-m resolution bedrock elevation map (resampled from 90 m SRTM data) arranged in a quadrilateral grid of nodal points over the Ohau LLGM ice catchment. Initial climate was defined by monthly temperature and precipitation values for New Zealand extracted from the WorldClim data set (Hijmans et al., 2005). WorldClim is a 1 km gridded AD1950-2000 climatology derived from the interpolation of a global array of weather station data using thin plate smoothing splines. This baseline modern climate input was adjusted in the LLGM simulations by shifting the temperature seasonal cycle according to prescribed anomalies (e.g., $\Delta T = -5$ °C implies 5 °C cooling), and by scaling precipitation (e.g., P = 75% implies 25% reduction). In order to account for evolving ice topography, the monthly temperature fields were modified using an atmospheric lapse rate of -5 °C km⁻¹, based on modern observations (Norton, 1985). However, we recognize that this is just a working scenario, as the value may have varied through time. In a sensitivity test of the LLGM Ohau glacier, we found that increasing the lapse rate to $-6\,^{\circ}\text{C km}^{-1}$ required only a $+0.2\,^{\circ}\text{C}$ $\Delta \textit{T}$ compensation relative to the -5 °C km $^{-1}$ baseline simulation in order to achieve the moraine-defined glacier footprint.

The climate signal is transferred to the ice-flow solver through a calculation of net annual surface mass balance, or the difference between snow/ice accumulation and ablation. This difference is obtained using a typical degree-day method (e.g., Braithwaite and Olesen, 1989). Although degree-day mass-balance schemes lack the complexity of energy-balance models (which consider spatial and temporal variations in albedo, insolation, and cloudiness), they are widely used in glacier modeling studies for their ease of implementation and overall good fit to observational data (Braithwaite, 2011). In our modeling, annual snow accumulation was determined by summing the precipitation amounts for all months when the temperature, T_{month} , is ≤ 0 °C. Ablation totals were generated by first summing melting degrees (md) (md_{month} = $T_{month} \times number$ of days in month) for all months when $T_{\rm month}$ is >0 °C. Accumulated snow was then reduced at a prescribed snowmelt rate (mm per md). If melting degrees remained once all winter snow had been ablated, ice was in turn melted at an ice-melt rate. We used melt factors for snow and ice of 4.6 and 7.2 mm md⁻¹, respectively, determined empirically for New Zealand (Anderson et al., 2006). Fig. 10 shows how choice of melt rates can influence snowline.

Ice sheet models such as UMISM have changeable parameters that to some extent control the behavior of ice flow. In order to

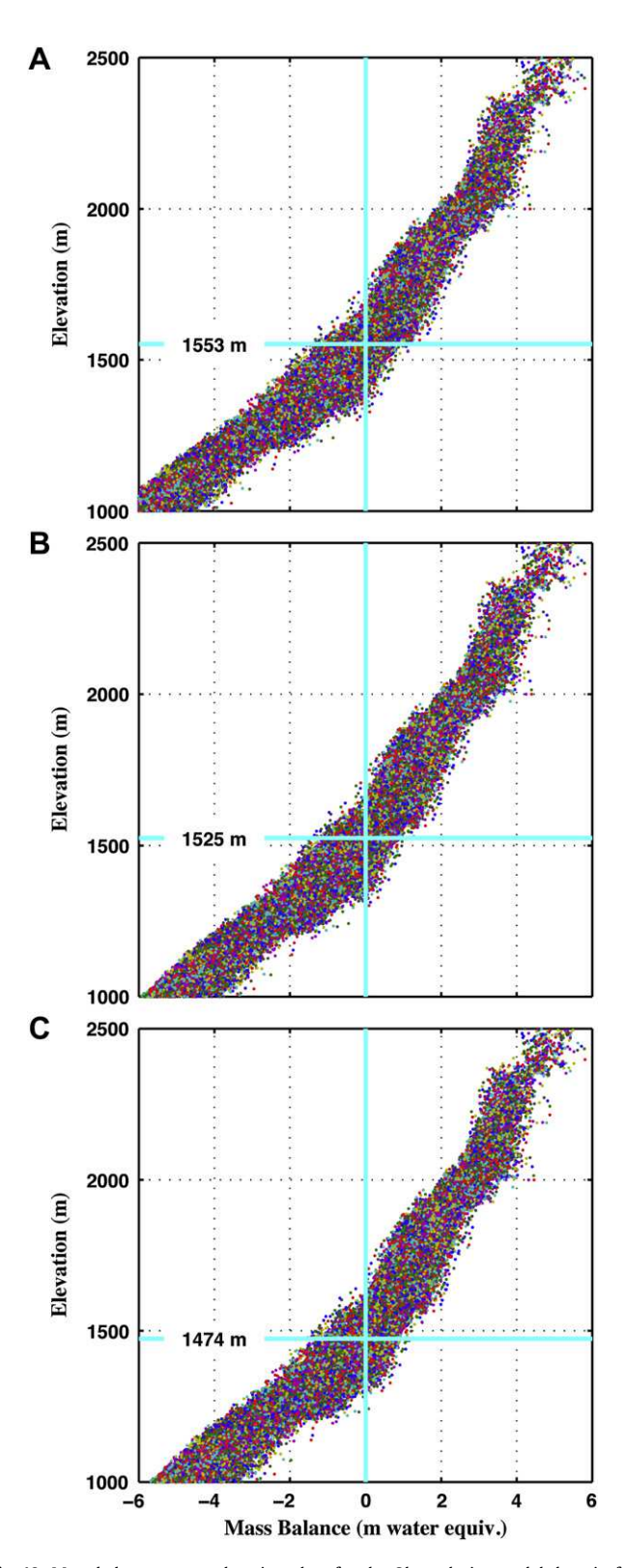


Fig. 10. Mass balance versus elevation plots for the Ohau glacier model domain for three different snow/ice melt rate (SMR/IMR) regimes with base climate at $\Delta T = -6.2$ °C, P = 100%, and atmospheric lapse rate = -5 °C km $^{-1}$. A) SMR = 4 IMR = 7, B) SMR = 4.6 IMR = 7.2, and C) SMR = 5 IMR = 8 (units mm md $^{-1}$). Snowline, denoted by blue lines, ranges 1474-1553 m, which affords an uncertainty of ± 50 m relative to the 1525 m value derived from New Zealand-specific degree-day factors. Further tests indicate that a 50 m rise or fall in snowline can be compensated by changing $\Delta T \sim 0.25$ °C. (For interpretation of the references to color in this figure legend, the reader is referred to the web version of this article.)

produce meaningful paleo-glacier reconstructions, it is therefore necessary to tune the model so that output is consistent with existing observational data. The chief ice-flow parameter tuned for this study was the sliding law constant, B (see Appendix). The value of B can be adjusted either to lessen or increase the amount of basal sliding due to melting and refreezing over rough beds. Low values afford relatively thin, fast-flowing ice, whereas high values afford the opposite. Another parameter, E, the ice-flow enhancement factor, can be tuned in order to change ice hardness to account for impurities. However, we left E at 1 (i.e., no flow enhancement) because similar net functionality is achieved by varying the sliding law constant.

Our experimental approach included more than a dozen sensitivity tests wherein ΔT was adjusted systematically for three scenarios of ice properties, defined by $B=0.02,\ 0.03,\$ and 0.04 (Fig. 10). Success or failure was determined by whether or not the modeled Ohau glacier expanded to LLGM moraine limits. We also tested cases for two precipitation scenarios, P=100% and P=70%. The latter value accounts for hypothesized drier climate over South Island during glaciations (Drost et al., 2007; Whittaker et al., 2011). Taken together, the results from these experiments provide a means to estimate probable temperature conditions across the Ohau glacier at the LLGM.

We note that our model is based on modern topography and lake-floor bathymetry, and it does not incorporate the effects of buried glacier trough geometry. We therefore take only the Ohau II/III simulation as generally indicative of LLGM ice extent and do not attempt to quantify a climatic value for the slightly shorter glacier length represented by the Ohau IV/V moraine belts. In addition, because we do not know whether or not the receding Ohau glacier was in equilibrium with climate when it exposed the bedrock bench at the Hopkins/Dobson confluence, we did not use the glacier model to estimate climatic conditions associated with that recession, but instead characterized the deglaciation of the Ohau valley using glacier-length changes inferred from geomorphology.

5. Results

5.1. ¹⁰Be surface-exposure dating

Results from ¹⁰Be sample analyses and procedural blank $^{10}\mbox{Be}/^{9}\mbox{Be}$ ratios are given in Table 1a and b, respectively. Procedural blanks indicate a contribution of 2100–21,600 contaminating ¹⁰Be atoms (Table 1b), with an average contribution of 9760 \pm 5307 atoms ($\pm 1\sigma$). Combined, corrections for contaminating ¹⁰Be (determined using procedural blanks) and boron were generally ~1%. Analytical uncertainties were typically 2–3%. Reported sample ¹⁰Be concentration uncertainties have been propagated with uncertainties in the measured blank ¹⁰Be concentration. All age calculations appear in Table 2, and have been referenced to calendar years BP (i.e., before AD1950, hereafter 'yrs' and 'yrs ago') by subtracting 56, 57, and 60 years for samples collected in AD2006, AD2007, and AD2010, respectively. Hereafter we discuss ages calculated using the 'Lm' scaling protocol [incorporating the highresolution geomagnetic model of Lifton et al. (2008), following Putnam et al. (2010b)] because this method yields results that tend to agree best with independent ¹⁴C constraints in the Southern Alps. A correction for geomagnetic effects integrated over the past 20,000 years is about 0.5%. Choosing alternative scaling methods or geomagnetic models to calculate ages yields agreement to within about 1.5%, and therefore would not affect any of the conclusions below. Uncertainties of elevations measured using differential global positioning system (GPS) are <1 m and thus have negligible effects on age uncertainties.

All exposure ages are plotted on maps in Fig. 11a and b. Based on the observed consistency of ages, we combined surface-exposure dates for each moraine belt (Fig. 12). We used χ^2 statistics to test the assumption that multiple ¹⁰Be dates from a single landform assemblage register coeval exposure to the cosmic-ray flux, representing the time of landform construction (Table 3). The χ^2 test analyzes whether dispersion among samples in each given data set can be explained by analytical uncertainties alone, or whether geomorphological factors, such as multiple episodes of deposition, predepositional (i.e., 'inherited') accumulations of cosmogenic ¹⁰Be, or post-depositional modification processes, have influenced a particular data set (Balco and Schaefer, 2006). 10Be surfaceexposure ages determined from Ohau III-V moraine belts exhibit low χ^2 values and hence high levels of internal consistency, implying that each belt of moraine landforms was constructed over a period that was within the uncertainty of the ¹⁰Be dating method as applied here.

Where distributions of individual ¹⁰Be ages for a group of associated landforms are approximately normal, we used Chauvenet's Criterion to test for statistical outliers at the 95% confidence level (Bevington and Robinson, 1992; Dunai, 2010). Outliers identified by this method were excluded from further statistical treatment. With the exception of ages from the Ohau I and II moraine belts, all other sample sets (Ohau III, IV, V, VI) have approximately normal distributions (Fig. 11). After removing outliers identified by the Chauvenet method, we calculated the arithmetic mean and standard deviation to provide a conservative measure of the landform age and associated uncertainty. We present all derived landform ages and uncertainties in Table 4.

Finally, systematic uncertainties attending ¹⁰Be production-rate and scaling protocols must be taken into account when evaluating the full range of acceptable landform ages. Because we use the local ¹⁰Be production rate of Putnam et al. (2010b), scaling uncertainties are negligible. Choosing a different ¹⁰Be production-rate value would shift all ¹⁰Be ages, and hence the whole moraine chronology, systematically. To illustrate the effects of production-rate uncertainties on the Ohau moraine chronology, we present in Table 4 'minimum' and 'maximum' possible landform ages calculated using the upper (+2.1%) and lower (-2.1%) error bounds, respectively, of the local ¹⁰Be production-rate (Putnam et al., 2010b). Landform ages are given below, and also presented in Table 4. It is important to note that landform ages should only be compared for a specific production-rate scenario. In the following presentation and discussion of landform assemblages, we use the mean age (third column of Table 4), based on the median value of the production-rate uncertainty range.

5.1.1. Ohau I

The three ages obtained from Ohau I moraines at Table Hill are between $\sim 130,000$ and 150,000 yrs (Figs. 11 and 12; Table 3), indicating deposition during Marine Isotope Stage 6. However, the ages are discordant (e.g., $\chi^2_{\rm experimental} = 23.42$ which is greater than $\chi^2_{\rm expected}$ of 5.99 at 95% confidence). One possibility is that the range is due to differential surface erosion of the boulders, thus the oldest age of 149,500 \pm 3100 yrs is closest to the true age of the moraine belt. However, the youngest sample came from a prominent moraine ridge that lies several ridges inboard of the ridge with the two older samples. Thus, another possibility is that these moraines are of composite age, and that the age spread is correct. We accommodate these possibilities conservatively, by suggesting a tentative age of 138,600 \pm 10,600 yrs, based on the arithmetic mean and standard deviation of the three dates. This age assignment is preliminary, pending further quantitative information of the age(s) of the Ohau I moraines.

CAMS laboratory no.	Sample ID	Latitude (DD)	Longitude (DD)	Elevation (m a.s.l.)	$ \begin{array}{l} \text{Boulder size} \\ (\text{L} \times \text{W} \times \text{H}) \\ (\text{cm}) \end{array} $	Sample thickness (cm)	Shielding correction	Quartz weight (g)	Carrier added (g) ^a	10 Be/ 9 Be $\pm 1\sigma$ $(10^{-14})^{b}$	$[^{10}\text{Be}] \pm 1\sigma$ $(10^4 \text{ atoms g}^{-1})^c$	Average ⁹ Be current (μA) ^d	AMS std ^e
Ohau I mor	aines												
BE24238	OH-07-04	-44.297439	169.98659	605.2	$240\times140\times120$	2.00	0.999	3.0021	0.2007	19.02 ± 0.45	84.28 ± 2.00	15.2(2)	07KNSTD _{B1,B2}
3E24240	OH-07-44	-44.297739	170.00296	615.4	$250\times150\times120$	1.19	0.999	5.0339	0.2008	22.34 ± 0.44	99.14 ± 1.95	13.6 (3)	07KNSTD _{B1,B2}
BE24241	OH-07-45	-44.298589	170.00239	621.1	$400\times330\times100$	1.89	0.999	5.0195	0.2014	20.60 ± 0.67	91.80 ± 3.02	15.0 (3)	07KNSTD _{B1,B}
Dhau II mo	raines												
3E23323	OH-06-60a	-44.35097	169.89591	599	$230\times220\times80$	1.81	0.999	4.0076	0.2031	7.42 ± 0.22	24.90 ± 0.75	11.6(3)	$KNSTD_{B3}$
3E23324	OH-06-61	-44.3489	169.89264	600	$160\times100\times60$	0.99	0.999	4.0054	0.1974	7.45 ± 0.22	24.31 ± 0.71	12.8 (3)	$KNSTD_{B3}$
BE24135	OH-06-62	-44.34733	169.90467	586	$220\times200\times90$	1.65	0.999	4.0033	0.2000	5.86 ± 0.19	19.30 ± 0.62	16.4(2)	$07KNSTD_{B4}$
3E23325	OH-06-63	-44.34317	169.90149	590	$320\times180\times60$	2.78	0.999	4.0186	0.2023	7.23 ± 0.27	24.09 ± 0.92	11.7 (4)	$KNSTD_{B3}$
BE27913	OH-07-01	-44.29125	169.98240	579	$320\times190\times144$	1.34	0.999	3.4861	0.1813	6.07 ± 0.18	20.94 ± 0.63	19.1 (4)	$07KNSTD_{B5}$
3E24136	OH-07-16	-44.31537	169.95898	569.1	$160\times120\times80$	2.01	0.987	4.0183	0.1995	5.44 ± 0.22	18.13 ± 0.73	7.9(4)	07KNSTD _{B4}
3E24137	OH-07-18	-44.31787	169.96605	564.5	$370\times330\times120$	1.34	0.999	4.0032	0.2023	5.14 ± 0.19	17.11 ± 0.65	10.0 (4)	$07KNSTD_{B4}$
3E24138	OH-07-19	-44.3236	169.97621	554.5	$200\times140\times90$	1.61	0.999	4.0156	0.2012	6.06 ± 0.22	20.04 ± 0.73	11.8 (4)	07KNSTD _{B4}
3E24139	OH-07-21	-44.32126	169.94935	570.5	$410\times400\times160$	1.45	0.999	4.0265	0.2002	6.35 ± 0.22	20.82 ± 0.74	13.3 (3)	$07KNSTD_{B4}$
E24239	OH-07-26	-44.341789	169.83328	680	$200 \times 190 \times 60$	2.35	0.999	3.0082	0.2012	4.73 ± 0.15	20.72 ± 0.69	15.2(3)	07KNSTD _{B1,B}
Dhau III mo	oraines												
3E22764	OH-06-04	-44.25613	169.98217	592.1	$190\times60\times160$	2.00	0.998	7.0417	0.1989	6.77 ± 0.18	12.59 ± 0.34	22.2(2)	$KNSTD_{BG}$
3E22912	OH-06-05	-44.25611	169.98219	591.6	$240\times170\times70$	0.96	0.999	7.0285	0.2035	8.33 ± 0.22	15.96 ± 0.43	17.9(2)	KNSTD _{B7}
3E22768	OH-06-16	-44.24982	169.97236	582.2	$210\times160\times100$	1.49	0.992	7.0495	0.1983	8.65 ± 0.21	16.05 ± 0.40	20.9(2)	$KNSTD_{B6}$
E22915	OH-06-18	-44.25058	169.97101	585.9	$100\times 60\times 70$	1.37	0.993	7.0649	0.1980	8.60 ± 0.25	15.96 ± 0.47	14.2(2)	KNSTD _{B7}
E22919	OH-06-44	-44.31698	169.94778	581.8	$280\times150\times180$	2.59	0.999	7.0605	0.2035	8.58 ± 0.33	16.37 ± 0.64	14.6 (4)	KNSTD _{B7}
E22927	OH-06-45	-44.32263	169.94554	574.2	$260 \times 120 \times 140$	1.88	0.999	7.0138	0.2026	8.95 ± 0.25	17.09 ± 0.48	14.4(3)	KNSTD _{B8}
3E22928	OH-06-46	-44.32507	169.94361	572.5	$220\times100\times60$	0.86	0.999	7.3478	0.2021	8.97 ± 0.23	16.31 ± 0.43	18.3 (2)	KNSTD _{B8}
BE22929	OH-06-50	-44.32681	169.9406	573.9	$130\times100\times80$	1.70	0.999	7.0161	0.1987	9.01 ± 0.28	16.87 ± 0.53	16.8 (3)	KNSTD _{B8}
BE23322	OH-06-59	-44.33402	169.88676	605	$400\times240\times170$	1.19	0.999	4.1080	0.2020	5.05 ± 0.15	16.41 ± 0.50	10.2 (5)	KNSTD _{B3}
E23326	OH-06-72	-44.33353	169.88824	602	$350\times320\times130$	1.5	0.996	4.0176	0.2018	4.81 ± 0.16	15.96 ± 0.53	11.2 (4)	$KNSTD_{B3}$
E23327	OH-06-73	-44.33335	169.88743	603	$450\times320\times90$	1.58	0.999	4.0301	0.1930	5.15 ± 0.20	16.29 ± 0.63	10.7 (5)	$KNSTD_{B3}$
3E24131	OH-07-08	-44.30317	169.95896	582.2	$260\times200\times200$	2.37	0.999	5.0339	0.2008	5.85 ± 0.22	15.33 ± 0.59	10.8(2)	07KNSTD _{B9}
BE24133	OH-07-10	-44.3041	169.9588	583.4	$400\times300\times310$	1.60	0.999	5.0195	0.2014	5.61 ± 0.15	14.84 ± 0.41	15.6 (3)	07KNSTD _{B4}
3E24134	OH-07-11	-44.30449	169.95875	581.7	$210\times200\times180$	1.65	0.999	5.0214	0.2008	4.92 ± 0.16	12.97 ± 0.43	17.8 (2)	$07KNSTD_{B4}$
3E24232	OH-07-13	-44.30615	169.95875	577.5	$270\times230\times180$	1.36	0.999	6.0094	0.1993	6.54 ± 0.21	14.26 ± 0.47	15.8 (2)	07KNSTD _{B1,2}
3E24233	OH-07-14	-44.30711	169.95823	576.9	$350\times220\times160$	1.18	0.999	5.0152	0.1983	5.79 ± 0.16	15.03 ± 0.44	15.4(3)	07KNSTD _{B1.2}
3E24234	OH-07-15	-44.30738	169.95822	575.5	$210\times110\times100$	2.01	0.999	5.0092	0.2012	5.59 ± 0.19	14.73 ± 0.53	15.2 (2)	07KNSTD _{B1,2}
E24235	OH-07-31	-44.33238	169.87581	620	$300\times170\times80$	1.92	0.998	5.0107	0.2005	5.67 ± 0.19	14.88 ± 0.52	15.6(2)	07KNSTD _{B1,2}
3E24128	OH-07-33	-44.33351	169.88021	618	$300 \times 90 \times 90$	0.87	0.999	5.0771	0.2015	6.12 ± 0.19	15.99 ± 0.52	14.7(2)	07KNSTD _{B9}
3E24129	OH-07-34	-44.33352	169.88027	618	$170\times110\times60$	1.48	0.999	5.0755	0.2002	6.07 ± 0.19	15.74 ± 0.50	15.4(2)	07KNSTD _{B9}
3E24130	OH-07-36	-44.33376	169.88213	613	$430\times250\times130$	0.88	0.989	5.0042	0.1986	6.03 ± 0.21	15.73 ± 0.54	12.9(2)	$07KNSTD_{B9}$
3E24226	OH-07-37	-44.33366	169.88232	613	$190\times100\times50$	1.04	0.999	5.013	0.2015	5.68 ± 0.15	15.04 ± 0.42	16.1(3)	07KNSTD _{B10}
E24236	OH-07-38	-44.33412	169.88575	606	$280\times210\times130$	0.91	0.999	5.0076	0.2002	5.62 ± 0.16	14.75 ± 0.44	15.3 (3)	07KNSTD _{B1,2}
3E24229	OH-07-39	-44.322689	169.87317	614	$280\times190\times70$	1.05	0.998	6.0114	0.1989	6.65 ± 0.22	14.47 ± 0.48	14.8 (2)	07KNSTD _{B1,2}
3E24230	OH-07-40	-44.323181	169.87543	612	$230\times200\times80$	1.02	0.999	6.0044	0.2009	6.77 ± 0.23	14.90 ± 0.51	16.5 (3)	07KNSTD _{B1,2}
E24231	OH-07-41	-44.323181	169.87543	612	$310\times 225\times 90$	1.79	0.999	6.0062	0.1988	6.91 ± 0.22	15.04 ± 0.48	15.5 (2)	07KNSTD _{B1,2}
hau IV mo	raines												
E24125	OH-06-08	-44.28244	169.94186	557.3	$370\times290\times50$	2.21	0.999	7.1038	0.2003	6.81 ± 0.20	12.65 ± 0.38	15.6(2)	$07KNSTD_{B9}$
E22913	OH-06-10	-44.27704	169.98217	561.4	$210\times160\times120$	2.07	0.998	7.0410	0.2011	6.77 ± 0.21	12.78 ± 0.40	15.9(2)	KNSTD _{B7}
BE22914	OH-06-11	-44.27659	169.94047	559.0	$300\times240\times120$	1.45	0.999	7.0320	0.1920	7.12 ± 0.24	12.85 ± 0.43	14.8 (4)	KNSTD _{B7}
3E22765	OH-06-13	-44.27492	169.93968	561.2	$230\times180\times100$	1.50	0.998	7.3979	0.1981	7.40 ± 0.19	13.05 ± 0.34	21.8 (2)	$KNSTD_{B6}$
3E22766	OH-06-14	-44.27046	169.93488	564.1	$280\times90\times110$	2.07	0.992	7.0396	0.1981	6.62 ± 0.18	12.26 ± 0.34	21.7 (2)	$KNSTD_{B6}$
E22767	OH-06-15	-44.269896	169.9301	546.3	$270\times180\times110$	1.13	0.992	7.0048	0.1985	6.89 ± 0.18	12.86 ± 0.34	22.3 (2)	$KNSTD_{B6}$
E22924	OH-06-22	-44.29886	169.90032	583.5	$550\times220\times400$	2.81	0.999	7.0591	0.2038	6.93 ± 0.21	13.19 ± 0.41	15.9 (2)	KNSTD _{B8}
E24126	OH-06-23	-44.29853	169.90072	583.6	$390\times260\times130$	1.55	0.999	7.0317	0.2013	6.42 ± 0.19	12.09 ± 0.37	15.4 (2)	07KNSTD _{B9}
3E22916	OH-06-24	-44.2974	169.90386	578.3	$280\times180\times210$	1.65	0.995	7.0789	0.2027	7.09 ± 0.23	13.42 ± 0.43	14.3 (2)	KNSTD _{B7}
E22926	OH-06-26	-44.29836	169.90023	575.3	$600\times400\times240$	1.27	0.999	7.0112	0.2035	6.94 ± 0.20	13.29 ± 0.39	17.8 (2)	KNSTD _{B8}

$\textbf{Table 1a} \ (continued \)$

CAMS laboratory	Sample ID	Latitude (DD)	Longitude (DD)	Elevation (m a.s.l.)	Boulder size $(L \times W \times H)$	Sample thickness	Shielding correction	Quartz weight (g)	Carrier added (g) ^a	10 Be/ 9 Be $\pm 1\sigma$ $(10^{-14})^{b}$	$[^{10}\text{Be}] \pm 1\sigma$ $(10^4 \text{ atoms g}^{-1})^c$	Average ⁹ Be current	AMS stde
no.					(cm)	(cm)						$(\mu A)^d$	
BE22917	OH-06-27	-44.29664	169.90778	579.2	400 × 250 × 360	3.33	0.999	7.0471	0.2037	7.09 ± 0.21	13.55 ± 0.41	16.5 (2)	KNSTD _{B7}
BE22770	OH-06-31	-44.29227	169.93141	546.8	$320\times280\times170$	1.92	0.998	7.0103	0.1978	6.92 ± 0.20	12.85 ± 0.37	19.3(2)	KNSTD _{B6}
BE24127	OH-06-84	-44.30176	169.87808	586.2	$310\times280\times100$	1.90	0.999	7.0804	0.1974	6.33 ± 0.19	11.61 ± 0.36	15.6(2)	$07KNSTD_{B9}$
BE22930	OH-06-85	-44.30282	169.88131	582.9	$410\times110\times220$	2.09	0.999	7.0090	0.1937	7.36 ± 0.21	13.41 ± 0.39	17.5 (2)	$KNSTD_{B8}$
BE22931	OH-06-86	-44.30214	169.89023	581.0	$280\times110\times110$	2.61	0.999	7.0289	0.1876	7.50 ± 0.22	13.21 ± 0.39	17.2 (2)	$KNSTD_{B8}$
BE23328	OH-06-90	-44.30577	169.89184	580	$130\times120\times90$	2.51	0.999	7.1630	0.2014	6.76 ± 0.21	12.52 ± 0.39	12.0(3)	KNSTD _{B8}
BE23329	OH-06-92	-44.3067	169.88222	580	$310\times130\times150$	2.87	0.999	7.0079	0.2017	6.63 ± 0.20	12.57 ± 0.38	11.6 (4)	KNSTD _{B8}
BE23330	OH-06-95	-44.30368	169.86948	591	$290\times150\times140$	1.68	0.999	7.0130	0.1988	7.25 ± 0.21	13.57 ± 0.40	11.7 (4)	$KNSTD_{B8}$
BE23331	OH-06-96	-44.30026	169.86005	598	$470\times230\times180$	1.00	0.998	7.0027	0.2008	6.70 ± 0.25	12.66 ± 0.47	13.1(2)	$KNSTD_{B8}$
Ohau V mo													
BE22925	OH-06-25	-44.29694	169.90352	575.7	$420\times230\times290$	1.36	0.999	7.0118	0.2037	6.66 ± 0.20	12.75 ± 0.39	17.5 (2)	$KNSTD_{B8}$
BE22769	OH-06-28	-44.29279	169.90362	554.8	$380\times220\times150$	1.94	0.998	7.0158	0.1978	6.47 ± 0.18	12.00 ± 0.34	21.5 (2)	$KNSTD_{B6}$
BE22918	OH-06-29	-44.29291	169.90602	550.1	$170 \times 160 \times 90$	1.35	0.999	7.0039	0.1999	6.62 ± 0.21	12.48 ± 0.39	16.2(2)	KNSTD _{B7}
BE22771	OH-06-78	-44.28507	169.87905	540.0	$730\times260\times220$	2.15	0.998	7.0248	0.1962	6.79 ± 0.15	12.48 ± 0.28	20.9 (4)	$KNSTD_{B6}$
BE22920	OH-06-79	-44.28508	169.87993	539.2	$250\times210\times130$	1.62	0.995	7.0228	0.2018	7.08 ± 0.21	13.45 ± 0.41	16.4(2)	KNSTD _{B7}
BE22772	OH-06-80	-44.28456	169.87991	539.0	$680\times430\times240$	1.78	0.998	7.0291	0.1974	6.77 ± 0.18	12.52 ± 0.33	23.2(2)	$KNSTD_{B6}$
BE22921	OH-06-88	-44.30005	169.88623	569.9	$240\times240\times140$	1.53	0.999	7.0364	0.1993	6.69 ± 0.16	12.52 ± 0.30	12.8 (4)	KNSTD _{B7}
Ohau VI mo													
BE29526	OH-10-01	-44.067938	169.866249	721.9	$300\times260\times50$	0.65	0.992	8.0589	0.1823	8.23 ± 0.14	12.50 ± 0.22	21.0 (4)	$07KNSTD_{B12}$
BE29527	OH-10-02	-44.068170	169.865613	718.8	$310\times260\times80$	1.30	0.992	7.9369	0.1820	7.99 ± 0.15	12.31 ± 0.24	15.8 (4)	$07KNSTD_{B12}$
BE29528	OH-10-03	-44.068120	169.865572	718.2	$250\times200\times90$	1.33	0.992	7.7802	0.1825	8.21 ± 0.16	12.93 ± 0.27	19.1 (3)	$07KNSTD_{B12}$
BE29521	OH-10-04	-44.069717	169.866875	694.0	$230\times120\times50$	1.19	0.993	7.7958	0.1837	8.20 ± 0.29	12.95 ± 0.46	17.2 (4)	07KNSTD _{B13}
BE29520	OH-10-05	-44.067300	169.865716	722.3	$205\times80\times40$	1.86	0.992	8.5528	0.1837	8.55 ± 0.21	12.32 ± 0.32	18.8 (3)	07KNSTD _{B13}
BE29519	OH-10-06	-44.067294	169.865681	722.3	$205\times115\times50$	3.14	0.992	7.8605	0.1826	7.81 ± 0.16	12.15 ± 0.26	17.9 (4)	07KNSTD _{B13}
BE29518	OH-10-07	-44.163124	169.813320	644.3	$185\times170\times60$	1.64	0.980	10.7265	0.1818	10.52 ± 0.23	11.94 ± 0.27	16.7 (4)	07KNSTD _{B13}
BE29593	OH-10-08	-44.172895	169.813869	622.4	$115 \times 170 \times 40$	2.19	0.982	10.3647	0.1816	6.37 ± 0.12	7.56 ± 0.15	20.0 (4)	07KNSTD _{B14,15}

a Carrier ⁹Be concentration is 996 ppm for all samples except for those labeled OH-10, for which the carrier ⁹Be concentration is 1024 ppm.

b Boron-corrected ¹⁰Be/⁹Be. Ratios are not corrected for background ¹⁰Be detected in procedural blanks.

c Reported [¹⁰Be] values have been corrected for background ¹⁰Be detected in procedural blanks.

d ⁹Be-³ measured after the accelerator. Reported currents are averaged over all AMS runs for a given sample. The number of AMS runs is given in parentheses.

e AMS standards to which respective ratios and concentrations are referenced. Reported ¹⁰Be/⁹Be ratios for KNSTD and 07KNSTD are 3.15 × 10⁻¹² and 2.85 × 10⁻¹², respectively (Nishiizumi et al., 2007). 'B' refers to corresponding procedural blank listed in Table 1b.

Table 1b Procedural blank ¹⁰Be data.

CAMS laboratory no.	Sample ID	Carrier added (g) ^a	$^{10} \text{Be} / ^9 \text{Be} \pm 1 \sigma (10^{-14})^b$	$N_{10_{\mathrm{Be}}}\pm1\sigma(10^3\ \mathrm{atoms})^{\mathrm{c}}$	Average ⁹ Be current (μA) ^d	AMS stde
BE24237	Blank1 17 Aug 07	0.2002	0.04 ± 0.02	5.1 ± 2.9	13.8 (3)	07KNSTD
BE24242	(B1) Blank2 17 Aug 07	0.2000	0.12 ± 0.03	16.4 ± 3.6	13.8 (2)	07KNSTD
BE23332	(B2) Blank 06 Jan 07	0.1987	0.04 ± 0.02	5.5 ± 2.1	10.4 (3)	KNSTD
BE24140	B3) Blank2 06 July 07	0.1929	0.06 ± 0.03	7.2 ± 3.9	17.0 (2)	07KNSTD
BE27919	(B4) Blank1 10 Nov 09	0.1789	0.02 ± 0.02	2.1 ± 2.6	16.7 (4)	07KNSTD
BE22763	(B5) Blank 04 Aug 06	0.1981	0.07 ± 0.01	10.2 ± 1.8	19.2 (3)	KNSTD
E22922	(B6) Blank 11 Sept 06	0.1988	0.08 ± 0.02	6.8 ± 2.3	15.5 (2)	KNSTD
BE22932	(B7) Blank 03 Oct 06	0.2029	0.06 ± 0.02	8.7 ± 2.2	14.9 (3)	KNSTD
BE24132	(B8) Blank1 06 July 07	0.2012	0.07 ± 0.02	9.8 ± 2.6	15.0 (2)	07KNSTD
E24214	(B9) Blank1 06 Aug 07	0.2021	0.07 ± 0.03	8.9 ± 4.4	17.9 (3)	07KNSTD
E24227	(B10) Blank2 06 Aug 07	0.2015	0.05 ± 0.02	6.2 ± 2.8	16.1 (3)	07KNSTD
E29537	(B11) Blank1 20 April 10	0.1824	0.15 ± 0.02	18.7 ± 2.9	16.7 (3)	07KNSTD
E29513	(B12) Blank1 29 April 10	0.1822	0.17 ± 0.02	21.6 ± 2.9	17.6 (3)	07KNSTD
E29594	(B13) Blank1 18 May 10	0.1816	0.08 ± 0.02	10.3 ± 2.4	14.1 (3)	07KNSTD
E29596	(B14) Blank2 20 May 10 (B15)	0.2004	0.06 ± 0.03	8.9 ± 4.1	18.0 (3)	07KNSTD

^a Carrier ⁹Be concentration is 996 ppm for all samples except for B13, B14, and B15, for which the carrier ⁹Be concentration is 1024 ppm.

^d ⁹Be⁺³ measured after the accelerator. Reported currents are averaged over all AMS runs for a given sample. The number of AMS runs is given in parentheses.

5.1.2. Ohau II

Ten ages from the Ohau II moraine ridges range from $26,350 \pm 1000$ to $33,860 \pm 1040$ yrs (Fig. 11) and form a bimodal distribution with a dominant peak (n = 6) and a younger secondary mode (n = 4) (Fig. 12). The dominant peak is centered at 32,500 yrs ago. The full distribution (no outliers removed) has an arithmetic mean of 30,810 \pm 2450 yrs (1 σ) and a median of 31,550 yrs. The distribution yields a $\chi^2=49.68$ which is greater than χ^2_{expected} of 16.92 at the 95% confidence level (Table 3), indicating that the data set includes multiple age populations (Balco and Schaefer, 2006). As boulder heights do not show a robust correlation to surfaceexposure age (R^2 < 0.01; see Section 6.1 below), and because there is no geomorphological evidence of landform degradation, we have no basis for inferring that post-depositional geomorphological processes have influenced the Ohau II age distribution. Two ages (OH-07-16 and OH-07-18) forming the young, secondary mode of the distribution come from remnants of moraines preserved as small islands in the Ohau III outwash plain, and it is conceivable that these remnants represent a younger moraine-forming event. The remaining two ages (OH-06-62 and OH-07-26) are not in morphostratigraphic order and are considered untenably young. To derive landform-age estimates we follow Ward and Wilson (1978) and separate the younger mode containing the two morphostratigraphically young ages from older mode. This procedure returned an age of 32,520 \pm 970 yrs (arithmetic mean of older population \pm 1 σ) for the outboard landforms and a tentative age of 27,400 \pm 1300 yrs ago (arithmetic mean of two morphostratigraphically consistent samples of the younger population \pm 1 σ) for inboard moraine remnants.

5.1.3. Ohau III

Twenty-six ages from the Ohau III moraine belt exhibit a high level of internal consistency (Figs. 11 and 12). The ages of two samples (OH-06-04 and OH-07-11) are identified as outliers by Chauvenet's Criterion and are excluded from further analysis. The resulting outlier-free distribution yields a χ^2 of 18.95 (Table 3),

^b Boron-corrected ¹⁰Be/⁹Be.

^c Total ¹⁰Be contamination (in atoms) determined from each procedural blank.

^e AMS standards to which respective ratios and concentrations are referenced. Reported 10 Be/ 9 Be ratios for KNSTD and 07KNSTD are 3.15 × 10⁻¹² and 2.85 × 10⁻¹², respectively (Nishiizumi et al., 2007).

Table 2 10 Be surface-exposure ages (in thousands of cal. yrs before AD1950, labeled 'ka', $\pm 1\sigma$) from the Lake Ohau moraines. Samples marked by a single asterisk (*) next to the sample ID are tentatively attributed to a younger episode of Ohau II moraine formation. Outlying ages are italicized and marked by a double asterisk (**) next to the sample ID. Bold ages ('Lm') are those discussed in text.

Sample ID	St age (ka)	De age (ka)	Du age (ka)	Li age (ka)	Lm age (ka)
Ohau I moraines	or age (mi)	20 age (na)	Da age (m)	z. age (ma)	z uge (nu)
OH-07-04	131.3 ± 3.2	130.1 ± 3.2	130.7 ± 3.2	129.7 ± 3.2	$\textbf{128.3} \pm \textbf{3.2}$
OH-07-04 OH-07-44	151.3 ± 3.2 153.2 ± 3.1	150.1 ± 3.2 151.6 ± 3.1	150.7 ± 3.2 152.3 ± 3.1	129.7 ± 3.2 151.1 ± 3.1	128.5 ± 3.2 149.5 ± 3.1
OH-07-44 OH-07-45	133.2 ± 3.1 141.4 ± 4.8	131.0 ± 3.1 139.9 ± 4.8	132.5 ± 3.1 140.6 ± 4.8	131.1 ± 3.1 139.4 ± 4.8	149.3 ± 3.1 138.0 ± 4.7
Ohau II moraines	141.4 ± 4.6	139.9 ± 4.8	140.0 ± 4.0	135.4 ± 4.6	130.0 ± 4.7
OH-06-60a	34.30 ± 1.05	34.35 ± 1.05	34.47 ± 1.05	34.40 ± 1.05	$\textbf{33.86} \pm \textbf{1.04}$
OH-06-61	33.26 ± 0.98	33.28 ± 0.98	33.42 ± 0.99	33.33 ± 0.99	32.80 ± 0.97
OH-06-62**	29.64 ± 0.97	29.61 ± 0.97	29.77 ± 0.97	29.65 ± 0.97	29.22 ± 0.95
OH-06-63	33.66 ± 1.30	33.70 ± 0.37	33.83 ± 1.31	23.03 ± 0.97 33.76 ± 1.31	33.21 ± 1.28
OH-07-01	32.60 ± 0.94	32.60 ± 0.94	32.75 ± 0.95	32.66 ± 0.94	33.21 ± 1.28 32.13 ± 0.98
OH-07-01 OH-07-16*	28.68 ± 1.17	28.68 ± 1.17	28.82 ± 1.18	28.72 ± 1.17	28.28 ± 1.15
OH-07-18*	26.68 ± 1.17 26.68 ± 1.02	26.71 ± 1.02	26.82 ± 1.18 26.85 ± 1.02	26.72 ± 1.17 26.76 ± 1.02	26.35 ± 1.00
OH-07-19	31.62 ± 1.17	31.62 ± 1.17	31.79 ± 1.17	31.68 ± 1.17	20.33 ± 1.00 31.17 ± 1.15
OH-07-13 OH-07-21	32.40 ± 1.17	32.41 ± 1.16	32.57 ± 1.17	32.47 ± 1.17	31.17 ± 1.13 31.94 ± 1.15
OH-07-21 OH-07-26**	29.58 ± 0.99	29.45 ± 0.99	29.59 ± 0.99	29.45 ± 0.99	29.11 ± 0.98
Ohau III moraines	29.56 ± 0.55	29.43 ± 0.93	29.39 ± 0.39	29.43 ± 0.33	23.11 ± 0.30
OH-06-04**	17.42 ± 0.48	17.63 ± 0.49	17.66 ± 0.49	17.71 ± 0.49	17.39 ± 0.48
OH-06-05	21.96 ± 0.60	22.07 ± 0.61	22.14 ± 0.61	22.13 ± 0.61	21.78 ± 0.60
OH-06-16	21.30 ± 0.00 22.48 ± 0.56	22.58 ± 0.56	22.66 ± 0.57	22.64 ± 0.57	21.78 ± 0.00 22.28 ± 0.56
OH-06-18	22.48 ± 0.56 22.25 ± 0.66	22.36 ± 0.66	22.43 ± 0.66	22.42 ± 0.66	22.28 ± 0.30 22.06 ± 0.65
OH-06-44	22.23 ± 0.00 22.93 ± 0.91	23.03 ± 0.00	22.43 ± 0.00 23.11 ± 0.92	23.08 ± 0.00	22.72 ± 0.90
OH-06-45	23.98 ± 0.68	24.06 ± 0.69	24.16 ± 0.69	24.11 ± 0.69	23.73 ± 0.68
OH-06-46	23.38 ± 0.08 22.74 ± 0.60	24.00 ± 0.09 22.85 ± 0.61	24.10 ± 0.03 22.94 ± 0.61	24.11 ± 0.03 22.91 ± 0.61	23.73 ± 0.08 22.54 ± 0.60
OH-06-50	23.63 ± 0.75	22.83 ± 0.61 23.72 ± 0.75	22.94 ± 0.01 23.82 ± 0.75	22.91 ± 0.01 23.78 ± 0.75	22.54 ± 0.60 23.40 ± 0.74
OH-06-59	23.03 ± 0.75 22.31 ± 0.68	23.72 ± 0.73 22.41 ± 0.69	23.82 ± 0.75 22.49 ± 0.69	23.78 ± 0.75 22.47 ± 0.69	23.40 ± 0.74 22.12 ± 0.68
OH-06-39 OH-06-72	21.89 ± 0.74	22.41 ± 0.09 22.01 ± 0.74	22.49 ± 0.09 22.08 ± 0.75	22.47 ± 0.09 22.06 ± 0.74	22.12 ± 0.08 21.72 ± 0.73
OH-06-73	21.89 ± 0.74 22.25 ± 0.86	22.35 ± 0.87	22.43 ± 0.87	22.41 ± 0.87	21.72 ± 0.73 22.06 ± 0.86
OH-07-08	23.71 ± 0.92	23.79 ± 0.92	23.89 ± 0.92	23.85 ± 0.92	23.48 ± 0.91
OH-07-08 OH-07-10	23.71 ± 0.92 22.80 ± 0.64	23.79 ± 0.92 22.89 ± 0.64	23.89 ± 0.92 22.98 ± 0.65	23.83 ± 0.92 22.94 ± 0.64	23.48 ± 0.91 22.59 ± 0.63
OH-07-11**	19.94 ± 0.69	20.12 ± 0.69	20.17 ± 0.70	22.94 ± 0.04 20.19 ± 0.70	19.84 ± 0.68
OH-07-11	21.98 ± 0.73	20.12 ± 0.03 22.10 ± 0.73	20.17 ± 0.70 22.18 ± 0.74	20.19 ± 0.70 22.17 ± 0.74	21.81 ± 0.72
OH-07-13 OH-07-14	21.38 ± 0.73 23.14 ± 0.68	23.24 ± 0.69	23.33 ± 0.69	23.30 ± 0.69	21.81 ± 0.72 22.93 ± 0.68
OH-07-14 OH-07-15	23.14 ± 0.08 22.84 ± 0.82	23.24 ± 0.09 22.94 ± 0.83	23.03 ± 0.03 23.03 ± 0.83	23.00 ± 0.03 23.00 ± 0.83	22.63 ± 0.08 22.63 ± 0.82
OH-07-13 OH-07-31	22.34 ± 0.32 22.26 ± 0.79	22.34 ± 0.83 22.35 ± 0.79	23.03 ± 0.83 22.42 ± 0.79	23.00 ± 0.83 22.40 ± 0.79	22.05 ± 0.32 22.06 ± 0.78
OH-07-31	23.74 ± 0.77	23.79 ± 0.78	23.89 ± 0.78	23.84 ± 0.78	23.49 ± 0.77
OH-07-34	23.74 ± 0.77 23.46 ± 0.75	23.79 ± 0.78 23.52 ± 0.75	23.69 ± 0.76 23.61 ± 0.76	23.57 ± 0.76	23.49 ± 0.77 23.22 ± 0.74
OH-07-34 OH-07-36	23.71 ± 0.83	23.77 ± 0.83	23.86 ± 0.83	23.82 ± 0.83	23.22 ± 0.74 23.47 ± 0.82
OH-07-37	22.44 ± 0.63	23.77 ± 0.63 22.53 ± 0.63	22.60 ± 0.63 22.61 ± 0.63	22.58 ± 0.63	$23.47 \pm 0.62 \\ 22.25 \pm 0.62$
OH-07-37 OH-07-38	22.44 ± 0.03 22.13 ± 0.67	22.23 ± 0.67	22.31 ± 0.67	22.38 ± 0.03 22.29 ± 0.67	21.94 ± 0.66
OH-07-38 OH-07-39	21.60 ± 0.73	21.72 ± 0.73	21.78 ± 0.74	21.78 ± 0.74	21.44 ± 0.72
OH-07-40	21.00 ± 0.75 22.26 ± 0.76	21.72 ± 0.73 22.35 ± 0.77	21.78 ± 0.74 22.43 ± 0.77	21.78 ± 0.74 22.41 ± 0.77	21.44 ± 0.72 22.07 ± 0.76
OH-07-40 OH-07-41	22.58 ± 0.73	22.66 ± 0.74	22.74 ± 0.74	22.71 ± 0.77 22.72 ± 0.74	22.38 ± 0.73
Ohau IV moraines	22.30 ± 0.73	22.00 ± 0.74	22.74 ± 0.74	22.72 ± 0.74	22.30 ± 0.73
OH-06-08**	19.95 ± 0.60	20.15 ± 0.61	20.20 ± 0.61	20.23 ± 0.61	19.86 ± 0.60
OH-06-10	18.16 ± 0.57	18.38 ± 0.58	18.42 ± 0.58	18.46 ± 0.58	18.12 ± 0.57
OH-06-11	18.20 ± 0.61	18.42 ± 0.62	18.46 ± 0.62	18.50 ± 0.62	18.15 ± 0.61
OH-06-13	18.47 ± 0.49	18.68 ± 0.50	18.72 ± 0.50	18.77 ± 0.50	18.41 ± 0.49
OH-06-14	17.47 ± 0.48	17.70 ± 0.49	17.73 ± 0.49	17.78 ± 0.50	17.44 ± 0.49
OH-06-15	17.47 ± 0.48 18.49 ± 0.50	18.71 ± 0.51	17.75 ± 0.43 18.75 ± 0.51	18.80 ± 0.51	17.44 ± 0.49 18.44 ± 0.50
OH-06-22	18.44 ± 0.58	18.65 ± 0.59	18.69 ± 0.59	18.73 ± 0.59	18.39 ± 0.58
OH-06-23	18.54 ± 0.58	18.74 ± 0.58	18.78 ± 0.59	18.82 ± 0.59	18.48 ± 0.58
OH-06-24	18.78 ± 0.61	18.98 ± 0.62	19.02 ± 0.62	19.06 ± 0.62	18.72 ± 0.61
OH-06-26	18.52 ± 0.55	18.73 ± 0.55	18.77 ± 0.56	18.81 ± 0.56	18.47 ± 0.55
OH-06-27	19.09 ± 0.58	19.29 ± 0.59	19.33 ± 0.59	19.37 ± 0.59	19.02 ± 0.58
OH-06-31	18.45 ± 0.53	18.67 ± 0.54	18.72 ± 0.54	18.76 ± 0.53	18.40 ± 0.53
OH-06-84	17.80 ± 0.55	18.01 ± 0.56	18.05 ± 0.54	18.09 ± 0.56	17.76 ± 0.55
OH-06-85	18.67 ± 0.55	18.87 ± 0.56	18.91 ± 0.56	18.96 ± 0.56	18.61 ± 0.55
OH-06-86	18.48 ± 0.55	18.69 ± 0.55	18.73 ± 0.55	18.77 ± 0.56	18.43 ± 0.55
OH-06-90	17.53 ± 0.56	17.75 ± 0.56	17.78 ± 0.56	17.83 ± 0.56	17.50 ± 0.55
OH-06-92	17.65 ± 0.54	17.75 ± 0.55 17.86 ± 0.55	17.90 ± 0.55	17.94 ± 0.55	17.61 ± 0.54
OH-06-95	18.72 ± 0.55	18.91 ± 0.56	18.95 ± 0.56	18.99 ± 0.56	18.65 ± 0.55
OH-06-96	17.30 ± 0.65	17.51 ± 0.66	17.54 ± 0.66	17.59 ± 0.66	17.27 ± 0.65
Ohau V moraines	17.50 ± 0.05	17.51 ± 0.00	17.51 ± 0.00	17.55 ± 0.00	17.27 ± 0.03
OH-06-25	17.77 ± 0.54	17.99 ± 0.55	18.02 ± 0.55	18.07 ± 0.55	$\textbf{17.74} \pm \textbf{0.54}$
OH-06-28	17.77 ± 0.54 17.11 ± 0.48	17.39 ± 0.33 17.34 ± 0.49	17.37 ± 0.49	17.43 ± 0.49	17.74 ± 0.34 17.09 ± 0.48
OH-06-29	17.11 ± 0.46 17.77 ± 0.56	17.34 ± 0.49 18.00 ± 0.57	17.57 ± 0.49 18.04 ± 0.57	17.43 ± 0.49 18.09 ± 0.57	17.09 ± 0.48 17.74 ± 0.56
OH-06-29 OH-06-78	17.77 ± 0.36 18.05 ± 0.41	18.28 ± 0.42	18.32 ± 0.42	18.37 ± 0.37 18.37 ± 0.42	17.74 ± 0.36 18.01 ± 0.41
OH-06-78 OH-06-79**					
OH-06-80	$19.47 \pm 0.60 \\ 18.08 \pm 0.48$	19.69 ± 0.60 18.31 ± 0.49	$19.74 \pm 0.60 \\ 18.35 \pm 0.49$	$19.78 \pm 0.60 \\ 18.40 \pm 0.49$	19.40 ± 0.59
OH-06-88		18.31 ± 0.49			18.04 ± 0.48 17.52 \pm 0.43
Ohau VI moraines	17.55 ± 0.43	17.77 ± 0.44	17.81 ± 0.44	17.86 ± 0.44	$\textbf{17.52} \pm \textbf{0.43}$
OH-10-01	17 17 0.20	17 30 ± 0.21	17.30 ± 0.31	17.36 ± 0.31	17 11 ± 0.20
OH-10-01 OH-10-02	$\begin{array}{c} 17.17 \pm 0.30 \\ 17.00 \pm 0.34 \end{array}$	$17.30 \pm 0.31 \\ 17.14 \pm 0.34$	17.30 ± 0.31 17.14 ± 0.34	17.36 ± 0.31 17.21 ± 0.34	$\begin{array}{c} \textbf{17.11} \pm \textbf{0.30} \\ \textbf{16.95} \pm \textbf{0.34} \end{array}$
011-10-02	17.00 ± 0.34	17.14 ± 0.34	17.14 ± 0.34	17.21 ± 0.34	10.33 ± 0.34

Table 2 (continued)

Sample ID	St age (ka)	De age (ka)	Du age (ka)	Li age (ka)	Lm age (ka)
OH-10-03	17.90 ± 0.37	18.03 ± 0.37	18.03 ± 0.37	18.09 ± 0.38	17.83 ± 0.37
OH-10-04	18.25 ± 0.66	18.38 ± 0.67	18.39 ± 0.67	18.45 ± 0.67	$\textbf{18.17} \pm \textbf{0.66}$
OH-10-05	17.05 ± 0.44	17.19 ± 0.45	17.18 ± 0.44	17.25 ± 0.45	$\textbf{17.00} \pm \textbf{0.44}$
OH-10-06	16.96 ± 0.37	17.10 ± 0.37	17.09 ± 0.37	17.16 ± 0.38	$\textbf{16.91} \pm \textbf{0.37}$
OH-10-07	17.77 ± 0.40	17.94 ± 0.41	17.96 ± 0.41	18.02 ± 0.41	$\textbf{17.72} \pm \textbf{0.40}$
OH-10-08**	11.44 ± 0.23	11.64 ± 0.24	11.66 ± 0.24	11.71 ± 0.24	11.49 ± 0.23

which is less than a χ^2 of 35.17 expected for a normal population at the 95% confidence level. Because the sample population is normally distributed, and because all measures of central tendency show close agreement, we use the arithmetic mean \pm 1 σ landform age of 22,510 \pm 660 yrs for the prominent outer Ohau III moraines (Figs. 11 and 12). Because only the outer parts of this moraine belt are bouldery, we do not know whether this age is also representative of the middle to inner, presumed recessional, parts of the moraine belt.

5.1.4. Ohau IV

Nineteen ages from the outer ridges of the Ohau IV moraine belt (Fig. 11) are tightly distributed and form an approximately normal population (Fig. 12). The distribution yields a χ^2 of 20.48, which is

less than the expected value of 28.87 for a normal distribution of this size (Table 3). All measures of central tendency agree (Table 3). We identified one age (OH-06-08) as an outlier using Chauvenet's Criterion. After the outlier is removed, we use the arithmetic mean $\pm~1\sigma$ to assign a landform age of 18,220 $\pm~500$ yrs.

5.1.5. Ohau V

Seven ages from the Ohau V moraine ridges form an approximately normal distribution with one older age (OH-06-79; 19,400 \pm 590 yrs) forming a shoulder on the older tail of the summed probability curve (Fig. 12). The χ^2 determined for this data set is 10.46, which is less than the $\chi^2_{\rm expected}$ value of 12.59 for a distribution of this size, indicating that all sample variability can be explained by analytical uncertainty alone (Table 3). The age of

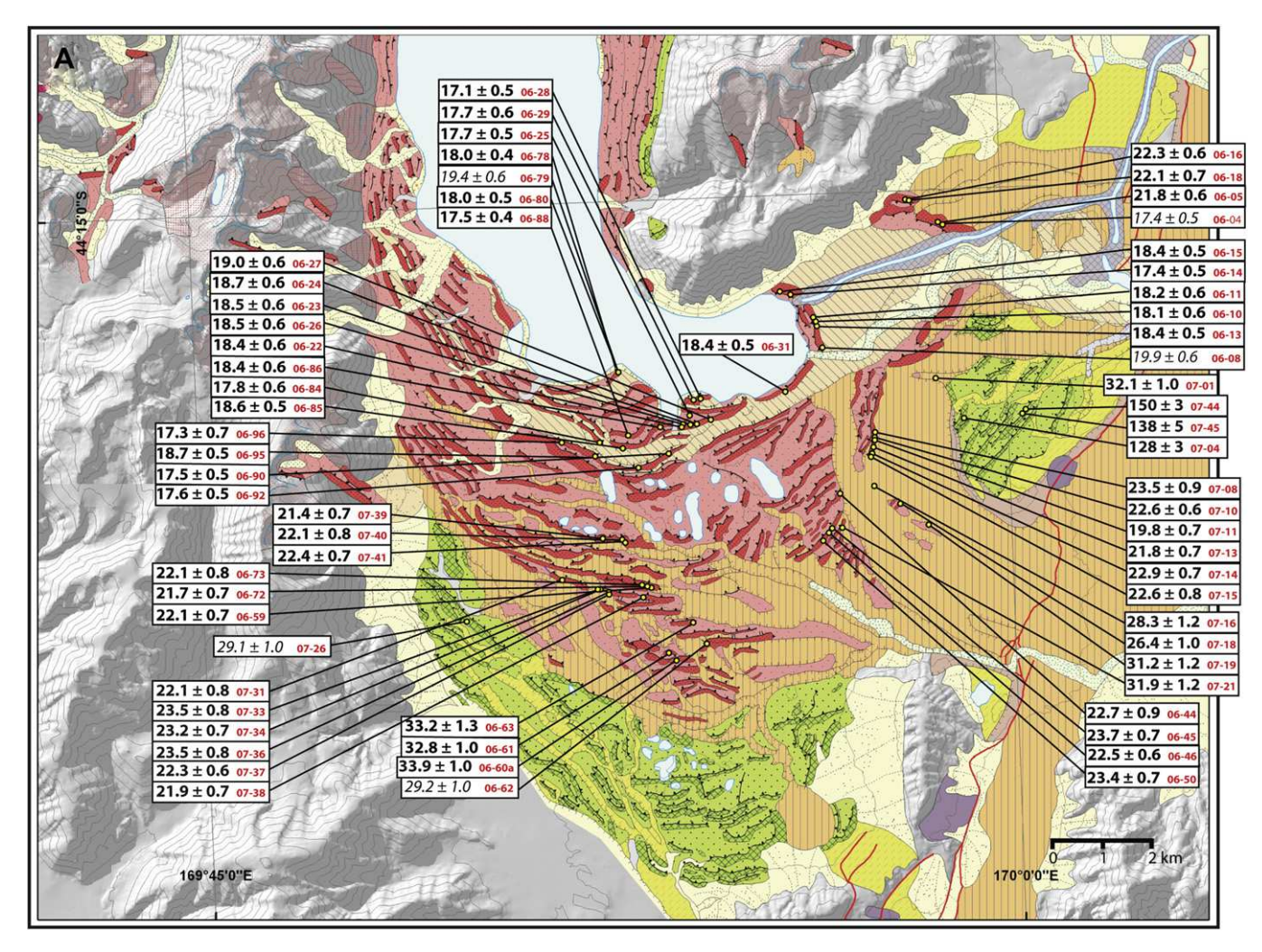


Fig. 11. Glacial geomorphologic map of Lake Ohau area. Panel A. Southern sector of field area. Panel B. Northern sector of field area. ¹⁰Be surface-exposure ages are in white boxes. Lines indicate sample locations. Ages (black text) are in ka ago. Italics denote ages that are statistical outliers (see text). Red text gives the last four digits of sample ID (Tables 1 and 2). Refer to Fig. 2 for geomorphologic legend and location context within the study area. (For interpretation of the references to color in this figure legend, the reader is referred to the web version of this article.)

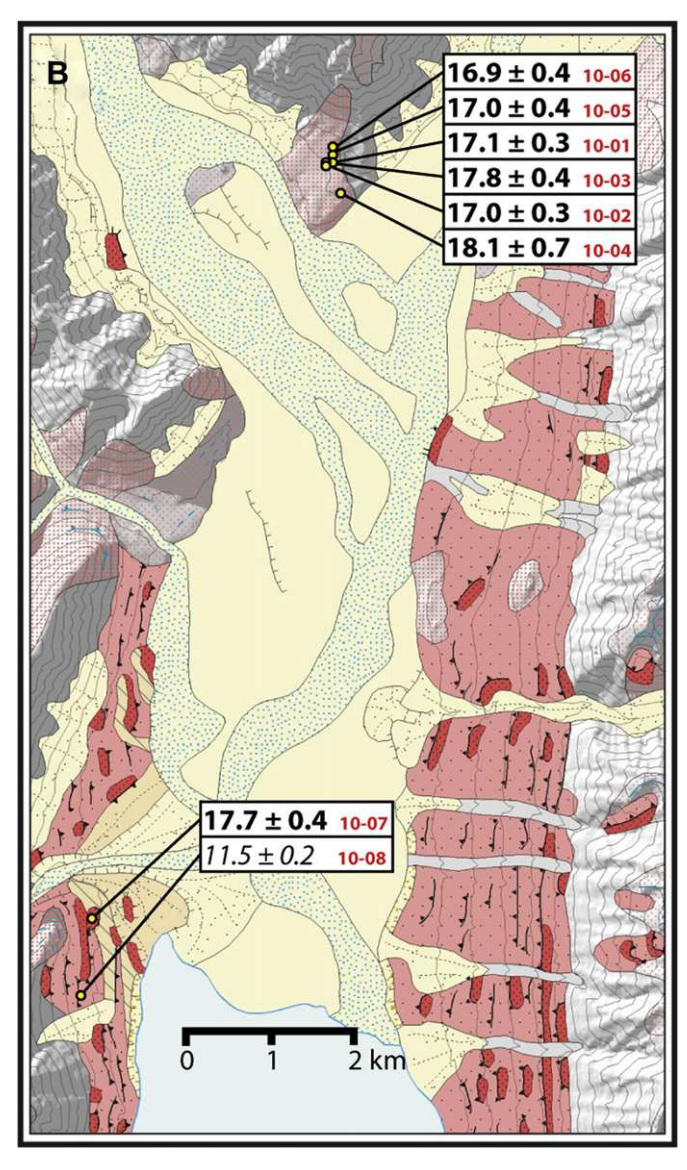


Fig. 11. (continued).

19,400 \pm 590 yrs that produces the shoulder of the distribution is identified as an outlier by Chauvenet's Criterion, and is therefore excluded from further analysis. After this outlier is removed, we assign an arithmetic mean \pm 1 σ age of 17,690 \pm 350 yrs for the Ohau V moraine ridges.

5.1.6. Ohau VI

Eight ages from Ohau VI recessional moraines and erratics on ice-molded bedrock form an approximately normal distribution, with one significantly younger age (OH-10-08; 11,490 \pm 230 yrs) identified as an outlier by Chauvenet's Criterion (Fig. 12). The full age distribution yields a $\chi^2_{\rm experimental}$ of 517.2, which is much larger than the $\chi^2_{\rm expected}$ value of 14.07, implying that the data set has been influenced by geomorphologic factors (Table 3). The boulder from which sample OH-10-08 was collected is near a talus slope at the base of a cliff face (Fig. 11), and it is possible that this boulder was emplaced by rock-fall 11,490 yrs ago, rather than by deposition from the receding glacier. Once this outlier age is removed the $\chi^2_{\rm experimental}$ for this data set is 8.48, which is less than the $\chi^2_{\rm expected}$ value of 12.59 for a data set of this size (Table 3). Based on this refined data set we assign an arithmetic

mean $\pm~1\sigma$ age of 17,380 $\pm~510$ yrs for the Ohau VI recessional morainal landforms.

5.1.7. Chronology of Irishman Stream landforms

Kaplan et al. (2010) reported 37 10 Be surface-exposure ages from the Irishman Stream moraines. All these ages were calculated in the same fashion as those reported in this study. Kaplan et al. (2010) assigned an age of 13,000 \pm 500 yrs ago (arithmetic mean \pm 1 σ) to the outermost Irishman Stream moraine ridge (Figs. 2 and 8). Younger moraines inboard were formed at 12,200 \pm 400 yrs ago and 11,500 \pm 400 yrs ago.

5.2. Glaciological modeling results

We conducted a series of 4000-year glaciological simulations to determine a probable range of ΔT for the LLGM Ohau glacier under physically plausible ice-flow regimes. In the first case we used modern precipitation values. Fig. 13 shows ice area, volume, and thickness results for optimum solutions R1, R2, and R3 with the sliding law constant set to 0.02, 0.03, and 0.04, respectively. In each of these simulations, the Ohau glacier grew to fit lateral and terminal moraine targets (Fig. 14). We obtained values of $\Delta T = -5.6$ °C in the case of relatively thin, fast flowing ice (R1), -6.5 °C for relatively thick, slow-moving ice (R3), and 6.2 °C for the middle condition (R2). Modern snowline averaged across the Ohau catchment in the model lies at 2458 m, and at 1478, 1525, and 1598 m for simulations R1, R2, and R3, respectively. Respective snowline depression values are 980, 933, and 860 m, with a midpoint of 920 \pm 50 m. The latter estimate is consistent with the 875 ± 50 m snowline depression estimated by Porter (1975) for the outer LLGM belt "Mount John" moraines of the nearby Lake Pukaki glacier trough. In a second set of simulations, we used the boundary conditions of R2, but reduced precipitation by 30%. From this we found that ice could meet LLGM lateral and terminal moraine targets only when ΔT equaled -6.9 °C.

Considering the full range of solutions reported above, we take the mid-point ΔT value of $-6.25\pm0.5\,^{\circ}\text{C}$ as a reasonable estimate of atmospheric temperature, relative to modern conditions, in the Ohau catchment during the LLGM. We note that our estimate of ΔT for the Ohau glacier is consistent with the -6 to $-6.5\,^{\circ}\text{C}$ estimate reported by Golledge et al. (2012) from a recent model of the whole Southern Alps icefield.

6. Geomorphological and glaciological implications of $^{10}\mathrm{Be}$ chronology

6.1. Post-depositional geomorphologic stability of Ohau landforms

Post-depositional moraine degradation can lead to boulder exhumation, which in turn can complicate interpretations of glacier history drawn from ¹⁰Be surface-exposure ages. Within the Ohau glacier landform assemblage, ¹⁰Be surface-exposure ages determined from boulders from the well-expressed moraine belts Ohau III, IV, and V show little variability beyond that which can be explained by analytical uncertainty alone (Table 3; Figs. 12 and 15). Although sampled boulders range from 50 cm to more than 400 cm tall, surface-exposure ages show no statistical correlation to boulder height (Fig. 15). Combined with observations of overall geomorphological stability of the Ohau landforms, we conclude that moraine degradation by diffusive processes (cf. Putkonen and Swanson, 2003; Applegate et al., 2012) has been negligible over at least the last $\sim 30,000$ yrs, and possibly since $\sim 150,000$ yrs ago. We therefore consider that landform ages derived here and discussed below can be confidently attributed to the timing of fluctuations of the Ohau glacier margin.

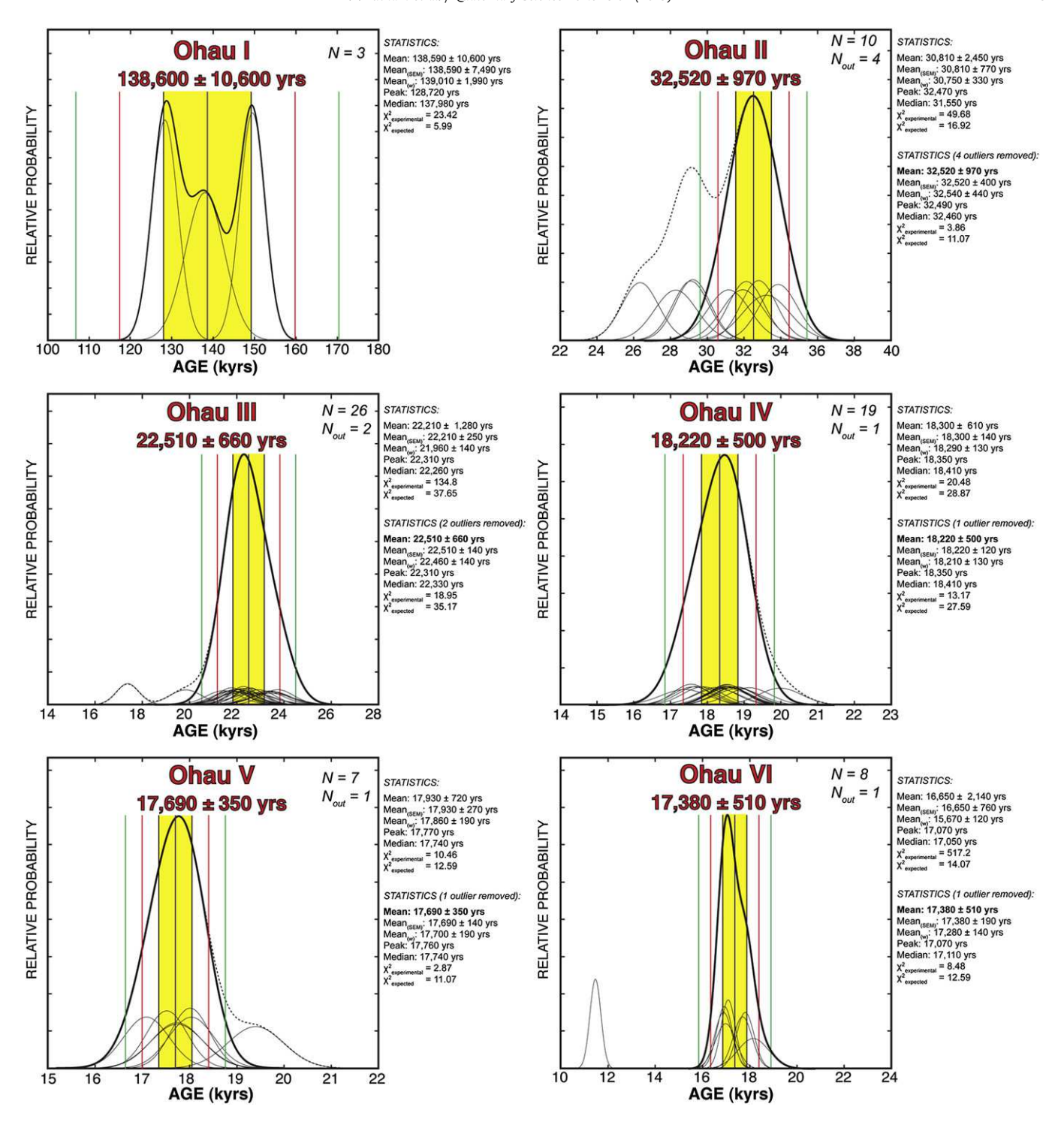


Fig. 12. Probability density functions (i.e., 'camelplots') for the six Ohau morainal landform assemblages. Center black line is arithmetic mean, while vertical black, red, and green lines are, respectively, 1σ, 2σ, 3σ uncertainty thresholds. Thin black curves are Gaussian curves representing individual samples. Dotted black line represents summed probability distribution for data set, including outliers. Thick black curve is summed probability distribution with outliers excluded. Statistics are inset. Note that the younger mode of the Ohau II distribution may reflect, at least in part, a later episode of moraine formation. (For interpretation of the references to color in this figure legend, the reader is referred to the web version of this article.)

6.2. Chronology of LLGM ice-margin fluctuations at Lake Ohau

The 10 Be chronology places the maximum LLGM extent of the Ohau glacier at 32,520 \pm 970 yrs ago, and affords inboard mean moraine dates of 27,400 \pm 1300 yrs ago, 22,510 \pm 660 yrs ago, 18,220 \pm 500 yrs ago, and 17,690 \pm 350 yrs ago. The \sim 22,500-yr Ohau III moraine belt served as a target for glaciological

modeling, which returned a snowline depression of 920 ± 50 m, and temperature lowering of 6.25 ± 0.5 °C, relative to modern values. The prominent geomorphological break separating Ohau III and IV implies that an interstade preceded construction of the Ohau IV moraines at $18,220\pm500$ yrs ago. Shortly after 18,000 yrs ago, following construction of the Ohau V moraines, the Ohau glacier evacuated the Lake Ohau basin. During this retreat, the Ohau glacier

Table 3Summary statistics for moraine ¹⁰Be surface-exposure age distributions. Ages are in cal. yrs before AD1950.

Data set	N	$N_{ m removed}$	Mean age (yrs)	±1σ (yrs)	Error-weighted mean (yrs)	Error-weighted uncertainty (yrs)	Standard error of the mean (yrs)	Peak age (yrs)	Median age (yrs)	$\chi^2_{ ext{experimental}}$	χ ² _{expected} (95%)	χ^2 test $(\chi^2_{\text{experimental}} < \chi^2_{\text{expected}})$
Ohau I (all)	3		138,590	10,600	139,010	1990	7490	128,720	137,980	23,42	5.99	Fail
Ohau II (all)	10		30,810	2450	30,750	330	770	32,470	31,550	49.68	16.92	Fail
Ohau II (no outliers)	6	4	32,520	970	32,540	440	400	32,490	32,460	3.86	11.07	Pass
Ohau III (all)	26	_	22,210	1280	21,960	140	250	22,310	22,260	134.8	37.65	Fail
Ohau III (no outliers)	24	2	22,510	660	22,460	140	140	22,310	22,330	18.95	35.17	Pass
Ohau IV (all)	19	_	18,300	610	18,290	130	140	18,350	18,410	20.48	28.87	Pass
Ohau IV (no outliers)	18	1	18,220	500	18,210	130	120	18,350	18,410	13.17	27.59	Pass
Ohau V (all)	7	_	17,930	720	17,860	190	270	17,770	17,740	10.46	12.59	Pass
Ohau V (no outliers)	6	1	17,690	350	17,700	190	140	17,760	17,740	2.87	11.07	Pass
Ohau VI (all)	8	_	16,650	2140	15,670	120	760	17,070	17,050	517.2	14.07	Fail
Ohau VI (no outliers)	7	1	17,380	510	17,280	140	190	17,070	17,110	8.48	12.59	Pass

produced the Ohau VI recessional moraines on the valley sides and exposed the glacially molded bedrock knob near the junction of the Hopkins and Dobson rivers. If it is assumed that the glacier terminus was located near the Hopkins/Dobson river confluence when the bedrock bench became exposed, this would imply a terminus retreat of \sim 24 km and hence a \sim 40% reduction in length of the Ohau glacier tongue over the approximately 300 yrs that had elapsed between construction of the Ohau V and VI landforms. Over the same time interval, the Ohau glacier surface lowered at least ~200 m to expose the Hopkins/Dobson River bedrock bench. Therefore, a mean net terminus retreat rate of \sim 77 m yr⁻¹ and ice-surface lowering rate of 0.7 m yr⁻¹ occurred between $\sim 17,700$ and $\sim 17,400$ yrs ago. Consideration of the longest possible duration of ice retreat, based on Ohau V and Ohau VI moraine age error limits, affords minimum net terminus retreat and ice-surface lowering rates of $\sim 20 \text{ m yr}^{-1}$ and 0.18 m yr⁻¹, respectively.

The Ohau glacier tributaries retracted well back into the high mountain valleys before a subsequent Lateglacial ice resurgence, documented by Kaplan et al. (2010) as culminating at $13,000 \pm 500$ yrs ago. Doughty et al. (2012) targeted the Irishman Stream Lateglacial moraines for glaciological modeling and determined that a snowline ~400 m lower than modern values and a ΔT of -2.7 ± 0.6 °C was necessary to grow the modeled glacier to the outer limit of the Lateglacial moraine belt. Thus, we consider from these results that the bulk of recession from LLGM moraine belts toward Lateglacial limits, indicating snowline rise and atmospheric warming of at least ~520 m and ~3.6 °C, respectively, took place within the first few millennia following the LLGM in the Lake Ohau drainage system of the Southern Alps of New Zealand. We note that evidence, if any, for the innermost limit of ice recession during the first pulse of deglaciation was masked by glacier readvance in Irishman Stream valley during the ACR. Thus, because the full distance of glacier recession prior to

Table 4Mean, maximum, and minimum landform ages based on systematic production-rate uncertainty limits. Production rate limits (PR_{max} and PR_{min}) are based on 'Lm' scaling and the production-rate uncertainty of $\pm 2.1\%$ (from Putnam et al., 2010b).

Data set	Basis for moraine age	Mean moraine age (PR _{mean}) (yrs)	Min. moraine age (PR _{max}) (yrs)	Max. moraine age (PR _{min}) (yrs)
Ohau I (all)	Chose: Mean \pm 1 σ ; Basis: Scattered small data set; considered general minimum age of moraine belt.	138,600 ± 10,600	≥135,680 ± 10,600	≤141,500 ± 10,820
Ohau II (old mode)	Chose: Mean $\pm 1\sigma$ after young mode $(n=4)$ removed. Basis: bimodal distribution.	$\textbf{32,} \textbf{520} \pm \textbf{970}$	\geq 31,840 \pm 950	\leq 33,200 \pm 990
Ohau II (young mode; outliers removed)	Chose: Mean $\pm 1\sigma$ after old mode $(n=6)$ and two morphostratigraphic outliers removed. Basis: bimodal distribution.	$27{,}400 \pm 1300$	\geq 26,820 \pm 1270	$\leq 27,980 \pm 1330$
Ohau III (outliers removed)	Chose: Mean $\pm 1\sigma$ after two outliers removed. Basis: Approx. normal distribution.	$\textbf{22,}\textbf{510} \pm \textbf{660}$	\geq 22,030 \pm 650	\leq 22,980 \pm 680
Ohau IV (outliers removed)	Chose: Mean \pm 1 σ after one outlier removed. Basis: Approx. normal distribution.	$\textbf{18,220} \pm \textbf{500}$	\geq 17,830 \pm 480	$\leq \! 18,\!600 \pm 510$
Ohau V (outliers removed)	Chose: Mean $\pm 1\sigma$ after one outlier removed. Basis: Approx. normal distribution.	$\textbf{17,690} \pm \textbf{350}$	$\geq\!17,\!320\pm350$	$\leq \! 18,\!060 \pm 360$
Ohau VI (outliers removed)	Chose: Mean $\pm~1\sigma$ after one outlier removed. Basis: Approx. normal distribution.	$\textbf{17,380} \pm \textbf{510}$	\geq 17,020 \pm 500	\leq 17,750 \pm 520

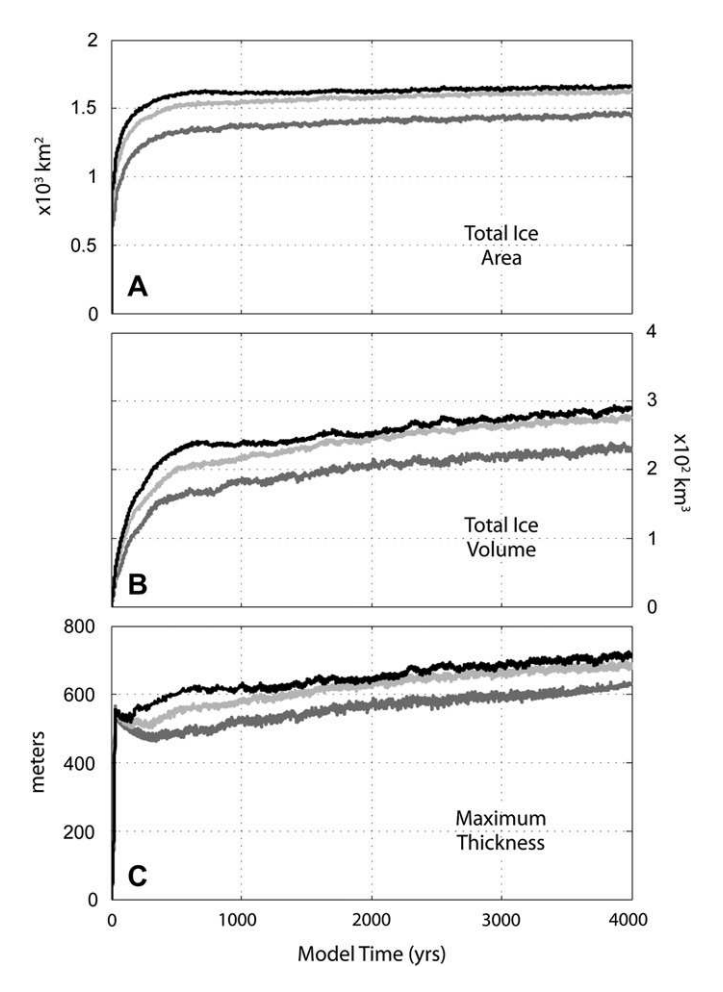


Fig. 13. A) Ice area, B) volume, and C) thickness results for three different ice-flow regimes defined by the sliding law constant in the Ohau glacier model domain: relatively thin, fast moving ice (R1, B = 0.02, dark gray); moderate ice (R2, B = 0.03, light gray); and thick, slow-moving ice (R3, B = 0.04, black).

the Lateglacial resurgence can not be discerned from geomorphology, we consider the magnitude of this snowline/temperature rise to be a minimum value.

7. Discussion

7.1. Comparison to other New Zealand glacier records and paleovegetation signatures

 10 Be dates of the youngest terminal moraines near Lake Ohau are consistent with those from the youngest LLGM moraines alongside Lake Pukaki, which lies $\sim\!20$ km northeast of Lake Ohau. Based on detailed 10 Be measurements near Boundary Stream on the right-lateral moraines of Lake Pukaki, the onset of ice withdrawal was 18,350 \pm 390 yrs ago (n=10, no outliers) (Putnam et al., 2010b). This age is indistinguishable from that of the Ohau IV moraine belt (18,220 \pm 500 yrs) that occurs alongside Lake Ohau. The 10 Be dates therefore suggest that the Pukaki glacier began a major recession about 18,000 yrs ago in concert with the Ohau glacier.

Well-documented and well-dated pollen records from lowland sites at Okarito, alongside the northwest flank of the Southern Alps on South Island west coast (Vandergoes et al., 2005; Newnham et al., 2007b), and Auckland, on northern North Island (Sandiford et al., 2003; Newnham et al., 2007a;

Augustinus et al., 2011), span the past $\sim 30,000$ yrs and complement the Ohau glacier record. These records show a distinct rise in the percentage of grass pollen, at the expense of shrub and tree pollen, beginning $\sim 29,000$ yrs ago. Over the following $\sim 11,000$ yrs the percentage of grass pollen varied, suggesting fluctuations between colder and milder conditions. A sustained shift in the pollen spectra began between $\sim 19,000$ and $\sim 18,000$ yrs ago, with progressive decline in grass pollen in favor of shrub and tree pollen, which became dominant at these lowland sites by $\sim 17,000$ yrs ago. Increasing dominance of shrub and tree pollen $\sim 18,000$ to $\sim 17,000$ yrs ago was commensurate with the onset of glacier recession from the Ohau and Pukaki LLGM moraine belts.

7.2. Comparison with records elsewhere in the Southern Hemisphere

As a test of whether the Ohau glacier record reflects general glacial conditions in the middle latitudes of the Southern Hemisphere, we compare the Ohau chronology with chronologies for LLGM glacier advances in mid-latitude South America (Figs. 16 and 17). In the Chilean Lake District (CLD; 39°–43°S), ¹⁴C ages assayed from plant macrofossils document times at which vegetated land surfaces were overrun by Andean piedmont glaciers and buried intact by glacial deposits (Denton et al., 1999b). The Last Glaciation terminal moraine complexes were formed by at least seven episodes of ice advance between ~36,000 and ~18,000 yrs ago (Fig. 15), and together these events comprise the LLGM of the CLD.

Formation of Ohau LLGM moraine belts match closely in time with glacier advances into the CLD LLGM moraine belts (Denton et al., 1999b) (Fig. 17). The age of the Ohau II moraine belt $(\sim 32,500-\sim 27,400 \text{ yrs})$ overlaps with the timing of glacier advances into the CLD LLGM moraine belt at 34,060 \pm 325 yrs ago (Puerto Octay site; n=5; no outliers), 31,120 \pm 70 yrs ago (Bahía Frutillar site; n = 17; 8 outliers excluded), and 27,910 \pm 210 yrs ago (Canal Tenglo site; n=6; 2 outliers excluded). Note that all ages given here for the CLD are from ¹⁴C dates reported in Denton et al. (1999b), converted to calendar ages using the IntCalO9 calibration curve (Reimer et al., 2009). The Last Glacial advance of the Corcovado ice lobe into the outer moraine belt on Isla Grande de Chiloe peaked at 18,035 \pm 215 yrs ago (Delcahue site; n = 34; 6 outliers excluded) (Denton et al., 1999b), coinciding with construction of the Ohau IV and V moraine belts at 18,220 \pm 500 and 17,690 \pm 350 yrs ago, respectively. Similar ages of ~18,000 yrs were obtained for the Last Glacial advance into the outer moraine belts of the Ancud, Reloncavi, and Llanquihue glacier lobes of the former Patagonian Ice Sheet in the CLD (Denton et al., 1999b).

The onset of deglaciation in the CLD (Denton et al., 1999b) began at approximately the same time as glacier recession at Lakes Ohau and Pukaki in the Southern Alps. In the CLD region, ice had receded to within ~ 10 km of modern glacier margins by $14,550 \pm 620$ yrs ago (Heusser, 1990). Farther south, on the east side of the Southern Andes at Lago Argentino ($\sim 50^{\circ} \mathrm{S}$), a readvance of a Southern Patagonian Icefield outlet glacier culminated at $\sim 12,990 \pm 80$ yrs ago (Strelin et al., 2011). Retreat occurred immediately thereafter, with ice receding to Holocene limits by $\sim 12,000$ yrs ago (Kaplan et al., 2011; Strelin et al., 2011). This Lateglacial signature of Patagonian glacier fluctuations mirrors that of the Irishman Stream tributary glacier in the Lake Ohau catchment (Kaplan et al., 2010) and those observed elsewhere in the central Southern Alps (Putnam et al., 2010a).

Paleoceanographic records (Fig. 16) also exhibit patterns similar to those defined from the Ohau moraine chronology. Alkenone-

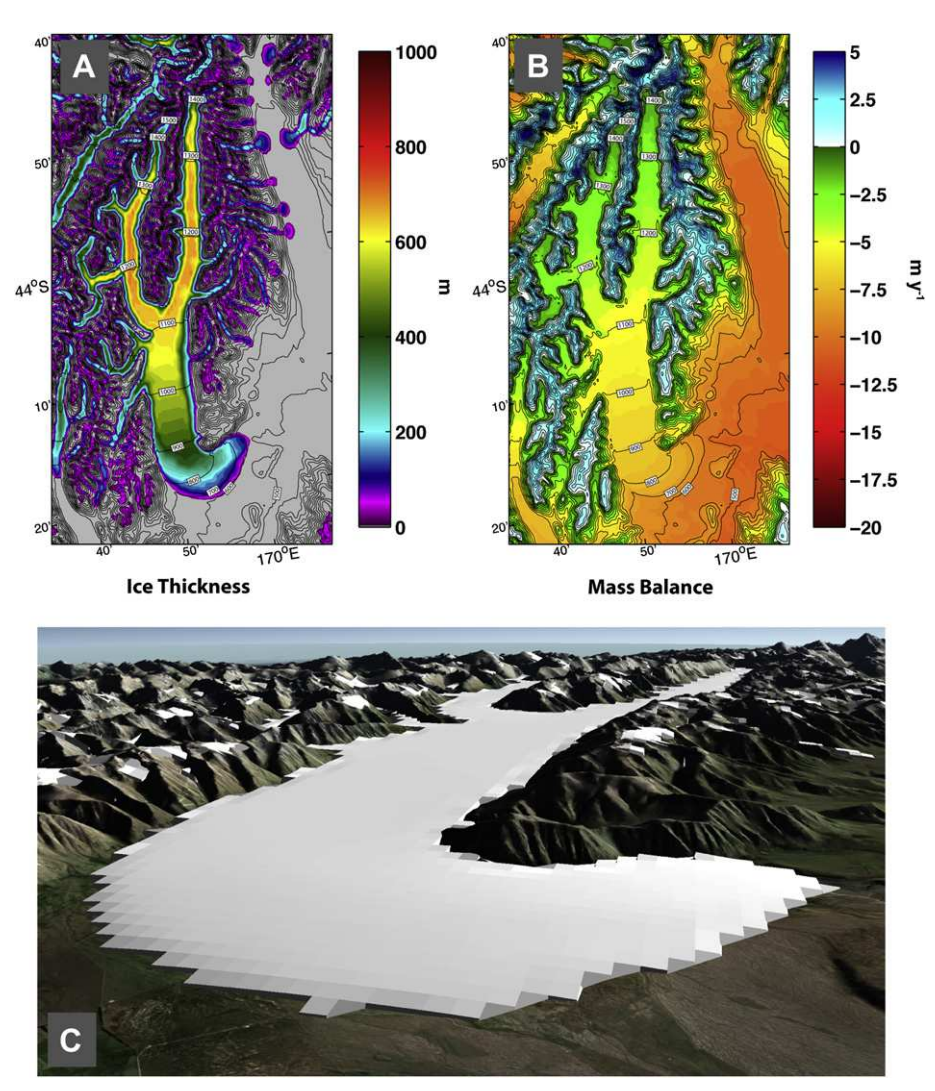


Fig. 14. Visualizations of simulation R2 at 4000 model years: A) ice thickness map, B) mass balance map, and C) shaded polygon surface rendered in Google Earth™. Model domain is fully specified for the Lake Ohau catchment only, and does not yield realistic results for neighboring catchments that are not fully included in the model domain. Elevation contours on the surface of the Ohau glacier are at 100 m intervals.

and Mg/Ca-inferred SSTs from cores off southern Australia (37°S; MD03-2611; Calvo et al., 2007) and Chile (41°S; ODP-1233; Lamy et al., 2004; Kaiser et al., 2005), as well as faunal-based SST reconstructions from the Indian Ocean (46°S; MD88-770; Labeyrie et al., 1996; Barrows et al., 2007), southeast Atlantic Ocean (41°S; TN057-21; Barker et al., 2009), and just west of South Island (42°S; SO136-GC3; Pelejero et al., 2006; Barrows et al., 2007) all record the onset of decline towards maximum glacial cold by $\sim 30,000 \text{ yrs}$ ago. The STF was equatorward of its present-day position during the LGM (Bard and Rickaby, 2009; Sikes et al., 2009; De Deckker et al., 2012). A cold and latitudinally expanded Southern Ocean persisted, with some variability, until ~ 18,000 yrs ago, after which time sea-surface warming commenced ubiquitously across the Southern Ocean (Lamy et al., 2004; Barrows et al., 2007; Calvo et al., 2007; Lamy et al., 2007; Barker et al., 2009; De Deckker et al., 2012).

The foraminiferal SST reconstructions from cores TNO57-21 at 41° S in the South Atlantic (Barker et al., 2009) and MD03-2611 at 37° S south of Australia (De Deckker et al., 2012) exhibit sharply expressed cold periods marking northward excursions of the STF that coincide with the construction of the Ohau III and IV moraine belts at \sim 22,500 and \sim 18,200 yrs ago, respectively (Fig. 17). Sea

surface warming and poleward migration of the STF commenced during the Ohau IV-VI recession phase (just after ~18,000 yrs ago), and which was interrupted by a SST/STF reversal that culminated coevally with construction of the Irishman Stream moraines at ~13,000 yrs ago. A final southern mid-latitude SST warming phase detected in cores TNO57-21 and MD03-2611 coincided with recession of the Irishman Stream glacier from Lateglacial to Holocene extents (\sim 13,000–11,700 yrs ago; Kaplan et al., 2010). The TNO57-21 and MD03-2611 faunal records also capture a prominent interstade, and southward movement of the STF, from \sim 21,000 to ~ 19,000 yrs ago that corresponds to the prominent geomorphological break between Ohau III and IV (i.e., after ~22,500 and before ~18,000 yrs ago), as well as the 'Varas Interstade' at \sim 21,000 to \sim 19,000 yrs ago in the Chilean Lake District (Mercer, 1972; Denton et al., 1999b). The observed close correspondence among millennial-scale events detected in SSTs and faunal assemblages south of Australia (Calvo et al., 2007; De Deckker et al., 2012), Atlantic SSTs (Barker et al., 2009), the Ohau glacier record presented here from the southwest Pacific region, and the CLD glacier record from the southeast Pacific, implies that all regions monitored a common Southern Hemisphere mid-latitude climate signal during the LLGM and Last Glacial termination.

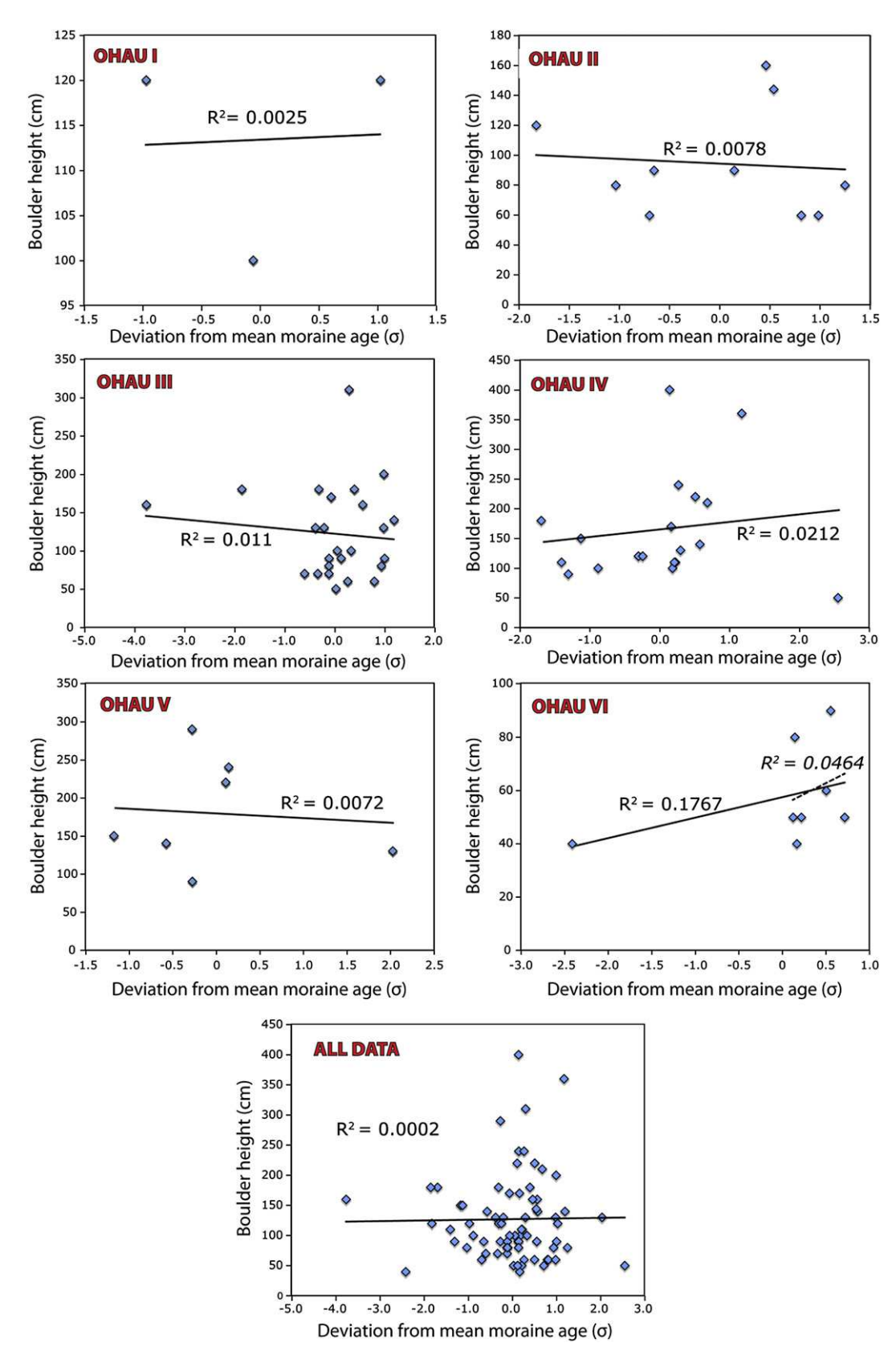


Fig. 15. Plots comparing boulder height versus ages normalized to mean moraine age for the six Ohau morainal landform assemblages. Bottom panel shows all data plotted together. Solid black lines show trend, with respective regression correlation coefficients plotted nearby (R^2 values). Dotted black line (and respective R^2 value) in Ohau VI panel gives resulting trend with one exceptionally young outlier age excluded from data set. Note that all data sets show no significant correlation between boulder height and boulder age.

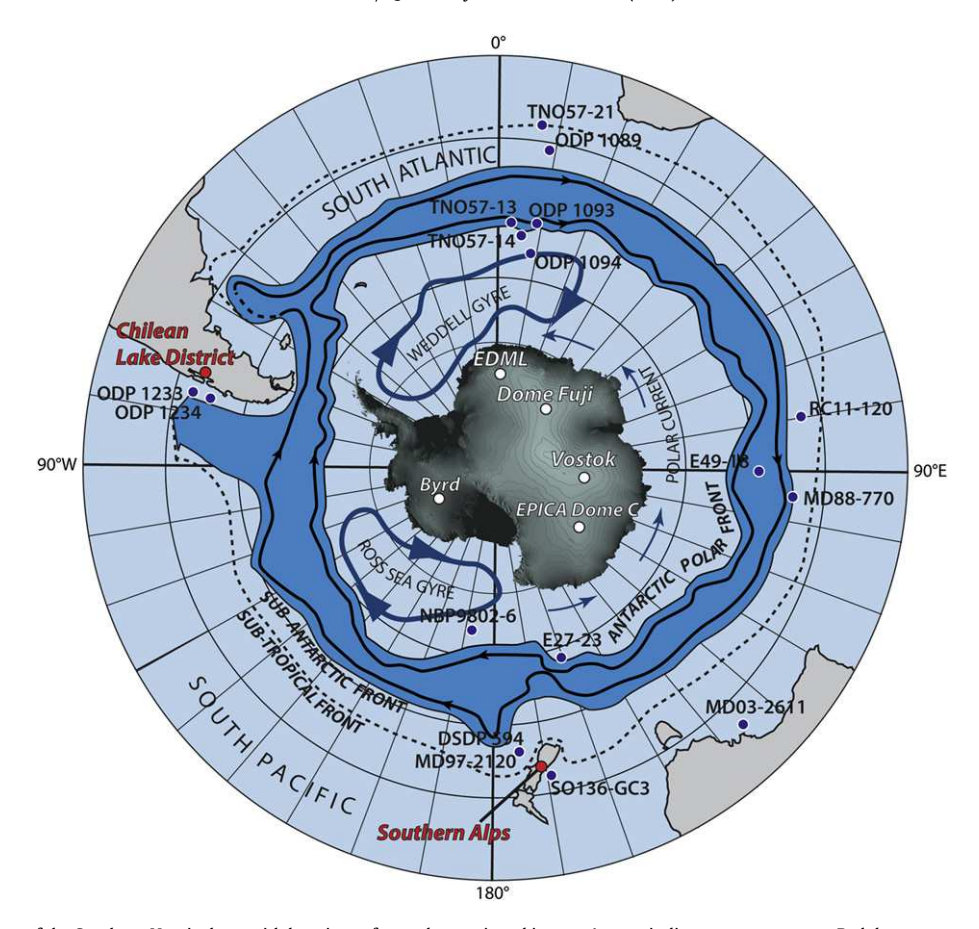


Fig. 16. Polar projection map of the Southern Hemisphere with locations of records mentioned in text. Arrows indicate ocean currents. Red dots are terrestrial sites discussed in text, blue dots give key marine sediment core locations, and white dots are locations of pertinent ice cores. Dark blue region illustrates sub-antarctic zone. Schematic physical oceanography adapted from Brown et al. (2001). (For interpretation of the references to colour in this figure legend, the reader is referred to the web version of this article.)

Furthermore, some aspects of the Ohau glacier record exhibit similarities to, as well as important differences from, Antarctic icecore isotope-inferred temperature records (~70–80°S; Petit et al., 1999; Blunier and Brook, 2001; EPICA Community Members, 2006; Kawamura et al., 2007; Lemieux-Dudon et al., 2010; see Fig. 16 for core locations). For example, the EPICA Dome C deuterium signature, placed on the timescale of Lemieux-Dudon et al. (2010), registered minimum ice-age temperatures over East Antarctica \sim 34,700 – \sim 17,900 yrs ago (Fig. 17), consistent with the duration of the Ohau LLGM. Antarctic warming commenced at \sim 17,900 yrs ago (Lemieux-Dudon et al., 2010), at the beginning of the last termination (Denton et al., 2010), in concert with the onset of deglaciation at Lakes Ohau and Pukaki. Resurgence of Southern Alps glaciers at 13,000 yrs ago fell within the Antarctic Cold Reversal (ACR) defined from Antarctic ice cores (Kaplan et al., 2010; Putnam et al., 2010a). Advances into the Ohau LLGM moraine belt also occurred during a period of persistently low atmospheric CO2 concentrations ~30,000-~18,000 yrs ago (Fig. 17; Monnin et al., 2001; Ahn and Brook, 2008). However, most Antarctic isotopeinferred temperature signatures do not register the strong millennial-scale variability during the LLGM evident in the Ohau glacier record, in the CLD glacier record (Denton et al., 1999a, 1999b), and in high-resolution SST reconstructions from southern middle latitudes (e.g., Barker et al., 2009). One exception is the δ¹⁸O-inferred atmospheric temperature signature from the EPICA Dronning Maud Land core (EPICA Community Members, 2006), which exhibits warming events that coincide with interstadial intervals indicated by the Ohau glacier record, the CLD glacier record, and southern mid-latitude SST patterns (Fig. 17).

Overall, southern mid-latitude SSTs records, as well as high-latitude ice-core signatures of atmospheric temperatures and CO₂, are concordant with the duration of sustained cold atmospheric temperatures as recorded by glaciers in the Southern Alps and southern South America (Fig. 17). Millennial-scale climate fluctuations were registered most strongly among mid-latitude records, with weak or absent counterparts in Antarctic ice-core isotope-inferred temperature records. Overall, most Southern Hemisphere paleoclimate data suggest that the ocean and atmosphere registered a common climate signal throughout the southern quarter of the globe during the LGM and beginning of the termination. Therefore, any proposed drivers of Southern Hemisphere climate must account for the long duration and the coeval termination of southern LGM conditions in both the ocean and the atmosphere, from 37°S to 77°S.

7.3. The LGM in the Southern Hemisphere

In seeking an explanation for Mercer's (1984) 'fly in the ointment' conundrum of an apparently synchronous LGM in the Northern and Southern Hemispheres, we look towards the Southern Ocean as a likely causative agent. The Southern Ocean has a propensity to stratify under cold atmospheric conditions (Gordon, 1991; Sigman et al., 2004), such as may arise from long-duration southern winters (Huybers and Denton, 2008; Keeling and Visbeck, 2011). Southern Ocean buoyancy-driven stratification results, at near-freezing water temperatures, from the density of seawater being more sensitive to changes in salinity than to changes in temperature (Sigman et al., 2004, 2010). Wintertime

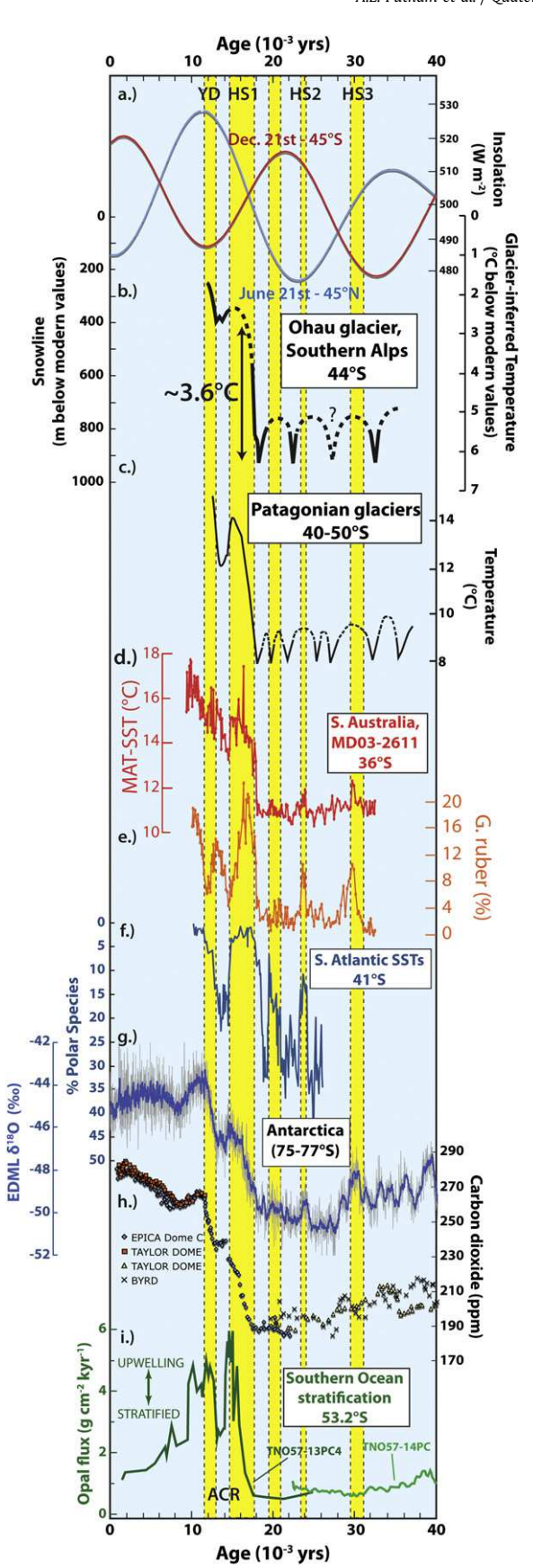


Fig. 17. Plot comparing records mentioned in text. a.) 45° N (blue) and 45° S (red) insolation intensity (Berger and Loutre, 1991). b.) Ohau glacier-inferred snowline and temperature reconstruction. This curve incorporates the Lateglacial reconstruction

cooling of surface water initiates sea-ice formation. Brine is rejected during winter sea-ice formation over the Antarctic continental shelf (Bouttes et al., 2010, 2011). Subsequent wind-driven export of sea ice into the open ocean promotes surface-water freshening and open-ocean stratification (Sigman and Haug, 2003). Thus winter cooling and sea-ice expansion play essential roles in spreading stratification into the Southern Ocean. Stratification cools the surface of the Southern Ocean by inhibiting upwelling of relatively warm deep waters (Gordon, 1981), enhancing the spread of winter sea ice. Any associated northward movement of the southern westerly wind belt would further reduce upwelling (Toggweiler et al., 2006; Toggweiler, 2008, 2009).

Collectively, marine proxies indicate that the Southern Ocean entered a fully stratified state as early as 70,000 years ago (Robinson et al., 2007; Anderson et al., 2009), consistent with increasing winter duration at that time. Opal records from the Antarctic Polar Front (Anderson et al., 2009), as well as records of % C. davisiana from the subantarctic zone (Hays et al., 1976), indicate that the Southern Ocean then remained in a generally stratified state, despite millennial-scale disturbances of stratification between ~60,000 and ~36,000 yrs ago corresponding to Heinrich Stadials in the North Atlantic (Anderson et al., 2009). These disturbances were evidently unable to completely destratify the ocean and initiate deep convection (Sigman et al., 2007). The Southern Ocean entered a state of persistent full stratification ~36,000 yrs ago (Hays et al., 1976; Robinson et al., 2007; Anderson et al., 2009; Sigman et al., 2010; Burke and Robinson, 2012), which along with expanded winter sea ice around Antarctica (Gersonde et al., 2003, 2005; Allen et al., 2011), continued through the LGM.

We suggest that stratification in the Southern Ocean, modulated by the effects of Earth's orbit on high-latitude winter duration (Huybers and Denton, 2008), resulted in cold temperatures that affected adjacent regions. Thus, Southern Ocean stratification provides an explanation for the formation of Ohau glacier LLGM moraines commencing as early as $\sim\!32,500\,\rm yrs$ ago, and continuing through to $\sim\!18,200\,\rm yrs$ ago. Individual ice advance maxima of the Ohau glacier during this interval may reflect millennial-scale fluctuations within generally cold climatic conditions.

A difficulty with the Southern Ocean coupled sea-ice/stratification model is that, taken alone, the effects of winter duration do not explain why, at \sim 32,500 yrs ago, when southern high-latitude winter duration was relatively short, the Southern Ocean was stratified and the Ohau glacier was just as extensive as it was \sim 22,500 yrs ago, when winter duration was relatively long. Although we consider southern winter duration to be an underlying factor governing stratification and SSTs in the Southern Ocean, and hence southern mid-latitude glaciers, we note also that Southern Alps glaciers would also have been strongly influenced by

from Irishman Stream (Kaplan et al., 2010; Doughty et al., 2012). Solid black lines depict where age control is known. Dotted black lines are based on inference. c.) Patagonian glacier-inferred temperature changes (Denton et al., 1999a; Denton et al., 1999b). Curve has been updated to reflect the Lateglacial record of Strelin et al. (2011). d.) Modern analogue technique (MAT) SSTs and e.) G. ruber from core MD03-2611 south of Australia (De Deckker et al., 2012). The latter is a proxy for tropical water incursions south of Australia, which indicates when the STF is to the south. f.) South Atlantic SSTs (Barker et al., 2009). g.) EPICA Dronning Maud Land δ^{18} O (Antarctic temperature proxy) (EPICA Community Members, 2006). Thin gray curve connects raw data. Thick blue line is 10-pt moving average. h.) Atmospheric CO2 records of Monnin et al. (2001), Indermühle et al. (1999, 2000), and Ahn and Brook (2008), synchronized to GICC05 (Greenland methane) timescale (Barker et al., 2009). i.) Southern Ocean stratification/upwelling record inferred from biogenic opal flux measured in cores TN057-13PC and TN057-14PC (Anderson et al., 2009). Vertical yellow bands correspond with northern stadials (southern warming events) in Barker et al. (2009) and Bond et al. (1999), HS1, HS2, and HS3 correspond to Heinrich Stadials 1, 2, and 3, respectively. YD is Younger Dryas. ACR is Antarctic Cold Reversal. (For interpretation of the references to colour in this figure legend, the reader is referred to the web version of this article.)

the position of the STF upwind of South Island. Millennial-scale migrations of the STF could have overwhelmed the more subtle effects of winter duration at the northern edge of the Southern Ocean between 36,000 and 18,000 yrs ago (De Deckker et al., 2012). In addition, once stratified, the vertical structure of the Southern Ocean, and its sea ice, could remain robust enough to withstand disturbance by orbital forcing. Thus it seems that a more powerful mechanism would have been required to destratify the Southern Ocean and re-initiate deep ventilation (Sigman et al., 2007).

Before exploring mechanisms for disruption of Southern Ocean stratification, we summarize the argument thus far. We speculate that stratification in the Southern Ocean is driven fundamentally by orbital forcing, as shown by the marine records of Hays et al. (1976), in particular through the effect of high-latitude winter duration on sea-ice formation (Huybers and Denton, 2008). Orbitally lengthened winters would prolong the period during which sea ice is formed and exported to the open ocean by the circum-Antarctic wind field, thereby promoting stratification in the open Southern Ocean. Once formed, stratification appears difficult to disrupt. At about 23,000 yrs ago, northern high-latitude summers were of low insolation intensity and southern lobes of the Laurentide Ice Sheet were at or near maximum extents (Lowell et al., 1999; Curry and Grimley, 2006; Curry and Petras, 2011), while southern highlatitude winters were of long duration (Huybers and Denton, 2008; Huybers, 2009), and the Ohau glacier was at or near its maximum extent. Thus, this mechanism, involving the effects of southern winter duration on Southern Ocean sea ice and stratification, resolves Mercer's (1984) conundrum, and offers an explanation for generally coeval maxima of the Ohau glacier and northern ice sheets during the global LGM, despite opposing summer insolation intensity patterns. This explanation circumvents any need for mysterious teleconnections between the hemispheres in order to account for global synchrony of the LGM. Future development of additional Southern Ocean stratification records from marine proxies could help to test the links between southern winter duration and stratification on orbital timescales.

We then come to the question of what brought about the end of the southern LGM? Retreat of the Ohau glacier occurred in unison with a regionally widespread warming trend, seen for example in SSTs (Barrows et al., 2007; Calvo et al., 2007; Barker et al., 2009), and indicated by disintegration of sea-ice cover around Antarctica (Shemesh et al., 2002; Allen et al., 2011). This southern warming coincided with Heinrich Stadial 1 (HS1) in the North Atlantic region (Bond et al., 1999; Barker et al., 2009; Denton et al., 2010). Thus, at face value, the southern warming beginning ~ 18,000 yrs ago had the hallmarks of an asynchronous millennial-scale climate oscillation between the North Atlantic and the Southern Ocean (Denton et al., 2010), involving an oceanic (Crowley, 1992; Broecker, 1998) and/or atmospheric (Toggweiler et al., 2006; Anderson et al., 2009) bipolar seesaw mechanism between the hemispheres (Sigman et al., 2007). However, on this occasion, a full glacial termination resulted. Taken together, modeling of the Ohau glacier (this study) and the Irishman Stream cirque glacier (Kaplan et al., 2010; Doughty et al., 2012) shows an overall warming between the LLGM and ACR of at least ~3.6 °C. Coeval phenomena included a net poleward migration of the southern STF (Chiessi et al., 2008; Bard and Rickaby, 2009; Sikes et al., 2009; De Deckker et al., 2012), rising atmospheric CO₂ (Monnin et al., 2001) and major upwelling south of the Polar Front (Anderson et al., 2009), which indicates breakdown of Antarctic stratification. Denton et al. (2010) pointed out that poleward migration of the wind-driven southern STF is difficult to explain solely by an oceanic mechanism, and proposed that a southward shift of the southern westerlies at the onset of HS1 stimulated a poleward shift of the southern STF (Denton et al., 2010; De Deckker et al., 2012). This southward shift of the

westerlies (Anderson et al., 2009), perhaps combined with the effects of a bipolar seesaw operating through the interior of the ocean (Broecker, 1998; Sigman et al., 2007), completely disrupted the stratification of the glacial Southern Ocean, and thereby triggered the last mountain glacier termination in Southern Hemisphere middle latitudes.

In conclusion, we suggest that the ice-age signature as reflected in the Ohau LLGM record, arose fundamentally from orbitally driven changes in southern high-latitude winter duration that, in turn, influenced stratification of the Southern Ocean. Previous studies have established relationships between Southern Ocean stratification and SSTs (Hays et al., 1976; Anderson et al., 2009). We propose that a prolonged episode of Southern Ocean stratification promoted generally cold southern mid-latitude atmospheric temperatures, and hence full-glacial icefields, during the global LGM. We then suggest that a bipolar seesaw oscillation, perhaps operating through both the atmosphere and the ocean, caused poleward migration of the southern STF and disruption of Southern Ocean stratification beginning at 18,000 yrs ago, resulting in seasurface warming that produced the southern mid-latitude Last Glacial termination.

8. Conclusions

- 1.) A precise and accurate 10 Be surface-exposure chronology, comprising 73 new dates on glacial landforms near Lake Ohau, as well as 37 previously reported dates from the Irishman Stream tributary of the Ohau catchment, indicates that the LLGM in the Southern Alps was achieved as early as $32,520\pm970$ yrs ago, and that subsequent glacier advances produced slightly inboard moraine belts at $27,400\pm1300$ yrs ago, $22,510\pm660$ yrs ago and $18,220\pm500$ yrs ago. Recession from the terminal moraine belt was underway by $17,690\pm350$ yrs ago, and by $17,380\pm510$ yrs ago, the Ohau glacier tongue had retreated by as much as ~24 km up valley. This retreat represents a $\sim40\%$ decrease of the LLGM glacier length and a net retreat rate of 77 m yr $^{-1}$. A glacier that fed the former Ohau glacier during the LLGM had receded well into the mountains by $13,000\pm500$ yrs ago (Kaplan et al., 2010).
- 2.) LLGM snowline was 920 ± 50 m below the present day value averaged across the Lake Ohau ice catchment. This snowline depression corresponds to a temperature depression of about 6.25 ± 0.5 °C, which is the median value determined from a variety of simulations in which flow parameters and precipitation were allowed to vary. Snowline and temperature rose by at least ~520 m and ~3.6 °C, respectively, between the LLGM and ACR
- 3.) Glacier variations at Lake Ohau complement marine and terrestrial records of climate change in the southern middle latitudes, as well as temperature and atmospheric CO₂ concentrations measured in Antarctic ice cores. We propose that enhanced sea ice and open-ocean stratification caused a decrease in Southern Ocean SSTs and an equatorward shift in the subtropical front that initiated the LLGM in the Southern Alps. We think that this Southern Ocean signal could have been paced in part by winter duration, which is sensitive to orbital precession, thereby producing the LLGM at Lake Ohau coevally with the maximum of the Laurentide Ice Sheet.
- 4.) We argue that a disruption of Southern Ocean stratification beginning ~18,000 yrs ago triggered the onset of the Last Glacial termination in the Southern Alps. We attribute this breakdown of stratification to a poleward shift of the southern westerlies, associated with HS1 cooling in the North Atlantic region (Denton et al., 2010). A southward shift of the southern STF and invigorated Southern Ocean upwelling led to an abrupt

onset of sea-ice retreat, SST warming, and CO_2 degassing, thereby warming Southern Hemisphere atmospheric temperatures and inducing mountain glacier retreat at Lake Ohau in the Southern Alps of New Zealand.

Acknowledgments

This work was supported by funding from the Gary C. Comer Science and Education Foundation (CSEF), the Ouesada Family Foundation, the National Oceanographic and Atmospheric Administration (NOAA), and by National Science Foundation grants EAR-1102782, EAR-0345835 and EAR-0745781. D.M. Sigman, S. Barker, W.S. Broecker, R.F. Anderson, T.J. Hughes, P. Huybers, B.L. Hall, G.R.M. Bromley, M.J. Vandergoes, P. Upton, and R.B. Alley provided helpful discussions. In particular, we are grateful to J.D. Hays for engaging discussions about the role of polar ocean stratification in ice-age cycles. N.R. Golledge, A.N. Mackintosh, B. Anderson, and T.J.H. Chinn contributed helpful insights into glaciological modeling in the Southern Alps. S. Barker kindly provided data from core TNO57-21. B. Lemieux-Dudon provided the updated EPICA Dome C chronology. K. Ladig and S. Travis helped with fieldwork. J. Frisch assisted with laboratory work. We are grateful to the Kees family (Ohau Station), F. Hawkins, M. Lindsay, J. Papich, G. Burrows (Ribbonwood Station), S. and H. Williamson (Glenbrook Station), J. and K. Wigley (Glen Lyon Station), and the Department of Conservation - Te Papa Atawhai, Te Rūnanga o Ngāi Tahu, for permitting us access to their land. T. and K. Ritchie of Lake Ruataniwha Holiday Park provided excellent accommodation during long field seasons. V. Jomelli and an anonymous reviewer provided helpful suggestions that improved the paper. A.E. Putnam was supported by CSEF, NOAA, a University of Maine teaching assistantship, and a Lamont-Doherty Earth Observatory (LDEO) postdoctoral fellowship while conducting this research. GNS Science's Direct Crown Funded Programme 'Global Change through Time' supported D.J.A.B. This is LDEO contribution #7629.

Appendix A

A complete description of UMISM can be found in Fastook and Prentice (1994) and Fastook et al. (2008). Here we provide an overview of the model ice-flow solver in order to give context for the tuning reported in the methods section. The tuning pertains to mainly the sliding and ice hardness terms below in Equations (2), (3) and (5).

The core of UMISM is a differential equation for ice extent and thickness as a function of time derived from an integrated momentum conservation equation based on the flow law of ice (Glen, 1955), coupled with a continuity equation for mass conservation:

$$\frac{\delta h}{\delta t} = MB - \nabla \cdot (UH), \tag{1}$$

where $\delta h/\delta t$ is the time-dependent ice-surface elevation, MB is the net-annual surface mass balance (accumulation minus ablation), U is the column-average ice velocity, and H is the ice thickness.

U in Equation (1) is obtained by expanding:

$$\dot{\varepsilon} = \left[\frac{\sigma}{A}\right]^n,\tag{2}$$

which is a tensor equation expressing strain rates, $\hat{\epsilon}$, and stresses, σ , through a non-linear power law. In this equation, n is the empirical flow law constant [we use a value of 3 for temperate glaciers

(Paterson, 1994)], and *A* is a temperature dependent function that represents ice hardness in an Arrhenius relationship:

$$A = EA_0 e^{-Q/RT}, (3)$$

where A_0 is a constant, Q is the activation energy for ice creep, R is the gas constant, T is the ice temperature, and E is a tuning (or flow enhancement) parameter meant to account for ice impurities.

By shallow-ice approximation, all stresses and strain rates are ignored in the force balance except basal drag. Thus, the stress in Equation (2) acting on the bed, or the "driving" stress, is expressed:

$$\sigma_{XZ} = \rho g H \nabla h, \tag{4}$$

where σ_{xz} is a stress in the *x*-direction acting on a surface with normal in the *z* direction, ρ is density of ice, *g* is gravitational acceleration, *H* is ice thickness, and ∇h is ice-surface slope.

Finally, U_1 is calculated from the sum of velocity due to internal deformation, U_D , and velocity due to basal sliding, U_S , as expressed:

$$U = U_{D} + U_{S} = \frac{2}{n+2} \left[\frac{\rho g \nabla h}{A} \right]^{n} H^{n+1} + \left[\frac{\rho g \nabla h}{B} \right]^{m} H^{m}, \tag{5}$$

where the last term follows a general sliding law relationship developed by Weertman (1964) for beds at the melting point, and modified to incorporate the effect of basal water (Johnson and Fastook, 2002). Here n is the empirical flow law constant in Equation (2), A is the ice hardness parameter described in Equation (3), B is the sliding law constant, and m is the sliding law exponent.

References

Ahn, J., Brook, E.J., 2008. Atmospheric CO_2 and climate on millennial time scales during the last glacial period. Science 322 (5898), 83–85.

Allen, C.S., Pike, J., Pudsey, C.J., 2011. Last Glacial—Interglacial sea-ice cover in the SW Atlantic and its potential role in global deglaciation. Quaternary Science Reviews 19–20, 2446–2458.

Amos, C.B., Burbank, D.W., Nobes, D.C., Read, S.A.L., 2007. Geomorphic constraints on listric thrust faulting: Implications for active deformation in the Mackenzie Basin, South Island, New Zealand. Journal of Geophysical Research 112. http:// dx.doi.org/10.1029/2006JB004291.

Amos, C.B., Burbank, D.W., Read, S.A.L., 2010. Along-strike growth of the Ostler fault, New Zealand: consequences for drainage deflection above active thrusts. Tectonics 29. TC4021.

Anderson, B., Mackintosh, A., 2006. Temperature change is the major driver of lateglacial and Holocene glacier fluctuations in New Zealand. Geology 34 (2), 121–124.

Anderson, B., Lawson, W., Owens, I., Goodsell, B., 2006. Past and future mass balance of 'Ka Roimata o Hine Hukatere' Franz Josef Glacier, New Zealand. Journal of Glaciology 52 (179), 597–607.

Anderson, R.F., et al., 2009. Wind-driven upwelling in the Southern Ocean and the deglacial rise in atmospheric CO₂. Science 323, 1443—1448.

Anderson, B., et al., 2010. Climate sensitivity of a high-precipitation glacier in New Zealand. Journal of Glaciology 56 (195), 114–128.

Applegate, P.J., et al., 2012. Improved moraine age interpretations through explicit matching of geomorphic process models to cosmogenic nuclide measurements from single landforms. Quaternary Research 77 (2), 293–304.

Augustinus, P.C., D'Costa, D., Deng, Y., Hagg, J., Shane, P., 2011. A multi-proxy record of changing environments from ca. 30 000 to 9000 cal. a BP: Onepoto maar palaeolake, Auckland, New Zealand. Journal of Quaternary Science 26 (4), 389–401.

Balco, G., Schaefer, J.M., 2006. Cosmogenic-nuclide and varve chronologies for the deglaciation of southern New England. Quaternary Geochronology 1 (1), 15–28.Balco, G., Stone, J.O., Lifton, N.A., Dunai, T.J., 2008. A complete and easily accessible means of calculating surface exposure ages or erosion rates from ¹⁰Be and ²⁶Al measurements. Quaternary Geochronology 4, 93–107.

Bard, E., Rickaby, R.E.M., 2009. Migration of the subtropical front as a modulator of glacial climate. Nature 460, 380–384.

 Barker, S., et al., 2009. Interhemispheric Atlantic seesaw response during the last deglaciation. Nature 457 (7233), 1097–1102.
 Barrell, D.J.A., Andersen, B.G., Denton, G.H., 2011. Glacial geomorphology of the

Barrell, D.J.A., Andersen, B.G., Denton, G.H., 2011. Glacial geomorphology of the central South Island, New Zealand. GNS Science Monograph 27. Lower Hutt, New Zealand. Map and 71 pp.

Barrell, D.J.A., 2011. Quaternary glaciers of New Zealand. In: Ehlers, J., Gibbard, P.L., Hughes, P.D. (Eds.), Quaternary Glaciations — Extent and Chronology, Part IV — a Closer Look. Developments in Quaternary Science. Elsevier, Amsterdam, pp. 1047–1064.

- Barrows, T.T., Juggins, S., De Deckker, P., Calvo, E., Pelejero, C., 2007. Long-term sea surface temperature and climate change in the Australian-New Zealand region. Paleoceanography 22, PA22215.
- Berger, A., Loutre, M.F., 1991. Insolation values for the climate of the last 10000000 years. Quaternary Science Reviews 10 (4), 297–317. Bevington, P., Robinson, D., 1992. Data Reduction and Error Analysis for the Physical
- Sciences. WCB McGraw Hill.
- Birkel, S.D., et al., 2012. Climate inferences from a glaciological reconstruction of the Late Pleistocene Wind River Ice Cap, Wind River Range, Wyoming. Arctic, Antarctic, and Alpine Research 44 (3), 265-276.
- Birkeland, P.W., 1982. Subdivision of Holocene glacial deposits, Ben Ohau Range, New Zealand, using relative-dating methods. Geological Society of America Bulletin 93, 443-449.
- Blunier, T., Brook, E.J., 2001. Timing of millennial-scale climate change in Antarctica and Greenland during the last glacial period. Science 291 (5501), 109-112.
- Bond, G.C., et al., 1999. The north Atlantic's 1-2 kyr climate rhythm: relation to Heinrich events, Dansgaard/oeschger Cycles and the Little Ice Age. Geophysical Monograph 112, 35-58.
- Bouttes, N., Paillard, D., Roche, D.M., 2010. Impact of brine-induced stratification on the glacial cycle. Climate of the Past Discussions 6, 575-589.
- Bouttes, N., et al., 2011. Impact of oceanic processes on the carbon cycle during the last termination. Climate of the Past Discussions 7, 1887-1934
- Braithwaite, R.J., Olesen, O.B., 1989. Calculation of glacier ablation from air temperature, West Greenland. In: Oerlemans, J. (Ed.), Glacier Fluctuations. D. Reidel Publishing Company, Dordrecht, p. 160.
- Braithwaite, R.J., 2011. Why do we expect glacier melting to increase under global warming? In: Blanco, J., Kheradman, H. (Eds.), Climate Change — Geophysical Foundations and Ecological Effects. InTech, p. 520.
- Broecker, W.S., van Donk, J., 1970. Insolation changes, ice volume, and the ¹⁸O record in deep-sea cores. Reviews of Geophysics 8 (1), 169-198.
- Broecker, W.S., 1966. Absolute dating and the astronomical theory of glaciation. Science 151, 299–304.
- Broecker, W.S., 1998. Paleocean circulation during the last deglaciation: a bipolar seesaw? Paleoceanography 13 (2), 119-121.
- Brown, E., et al., 2001. Ocean Circulation, second ed. The Open University.
- Burke, A., Robinson, L.F., 2012. The Southern Ocean's role in carbon exchange during the last deglaciation. Science 335, 557–561.
- Burrows, C.J., 2005. Julius Haast in the Southern Alps. Canterbury University Press, Christchurch.
- Calvo, E., Pelejero, C., De Deckker, P., Logan, G.A., 2007. Antarctic deglacial pattern in a 30 kyr record of sea surface temperature offshore South Australia. Geophysical Research Letters 34 (13), L13707.
- Carter, L., et al., 1998. Ocean Circulation New Zealand. In: NIWA Chart Miscellaneous Series, vol. 76. NIWA, Wellington.
- Chiessi, C.M., et al., 2008. South Atlantic interocean exchange as the trigger for the Bolling warm event. Geology 36 (12), 919-922.
- Chinn, T., Winkler, S., Salinger, M.J., Haakensen, N., 2005. Recent glacier advances in Norway and New Zealand: a comparison of their glaciological and meterological causes. Geografiska Annaler 87A, 141-157.
- Chinn, T.J., 1996. New Zealand glacier responses to climate change of the past century. New Zealand Journal of Geology and Geophysics 39, 415–428.
- Clark, P.U., Mix, A.C., 2002. Ice Sheets and sea level of the Last Glacial Maximum. Quaternary Science Reviews 21, 1-7.
- Clark, P.U., et al., 2009. The Last Glacial Maximum. Science 325, 710-714.
- Cox, S.C., Barrell, D.J.A., 2007. Geology of the Aoraki Area. 1:250,000 Geological Map 15. GNS Science. GNS Science, Lower Hutt, New Zealand, 1 Sheet and 71 pp. Crowley, T.J., 1992. North Atlantic deep water cools the Southern Hemisphere.
- Paleoceanography 7 (4), 489–497.
 Curry, B.B., Grimley, D.A., 2006. Provenance, age, and environment of mid-
- Wisconsinan slackwater lake sediment in the St. Louis Metro East area, USA. Quaternary Research 65, 108-122.
- Curry, B.B., Petras, J., 2011. Chronological framework for the deglaciation of the Lake Michigan lobe of the Laurentide Ice Sheet from ice-walled deposits. Journal of Quaternary Science 26 (4), 402-410.
- Davis, K., Burbank, D.W., Fisher, D., Wallace, S., Nobes, D., 2005. Thrust-fault growth and segment linkage in the active Ostler fault zone, New Zealand. Journal of Structural Geology 27 (8), 1528-1546.
- De Deckker, P., Moros, M., Perner, K., Jansen, E., 2012. Influence of the tropics and southern westerlies on glacial interhemispheric asymmetry. Nature Geoscience 5, 266-269.
- Dee, D.P., et al., 2011. The ERA-Interim reanalysis: configuration and performance of the data assimilation system. Quarterly Journal of the Royal Meteorological Society 137, 553-597.
- Denton, G.H., et al., 1999a. Interhemispheric linkage of paleoclimate during the last glaciation. Geografiska Annaler 81A (2), 107-153.
- Denton, G.H., et al., 1999b. Geomorphology, stratigraphy, and radiocarbon chro-nology of Llanquihue drift in the area of the southern Lake District, Seno Reloncaví, and Isla Grande de Chiloé, Chile. Geografiska Annaler 81A, 167–229.
- Denton, G.H., et al., 2010. The last glacial termination. Science 328, 1652-1656. Desilets, D., Zreda, M., Prabu, T., 2006. Extended scaling factors for in situ cosmogenic nuclides: new measurements at low latitude. Earth and Planetary Science
- Letters 246, 256-276. Doughty, A.M., et al., 2012. Late-glacial temperatures in the Southern Alps of New Zealand based on glacier modelling at Irishman basin. Quaternary Science
- Reviews. http://dx.doi.org/10.1016/j.quascirev.2012.09.013.

- Drost, F., Renwick, J., Bhaskaran, B., Oliver, H., McGregor, J., 2007. A simulation of New Zealand's climate during the Last Glacial Maximum. Quaternary Science Reviews 26, 2505-2525.
- Dunai, T., 2001. Influence of secular variation of the magnetic field on production rates of in situ produced cosmogenic nuclides. Earth and Planetary Science Letters 193, 197–212.
- Dunai, T.J., 2010. Cosmogenic Nuclides: Principles, Concepts, and Applications in the Earth Surface Sciences. Cambridge University Press, New York.
- EPICA Community Members, 2006. One-to-one coupling of glacial climate variability in Greenland and Antarctica. Nature 444 (7116), 195-198.
- Fastook, J.L., Prentice, M., 1994. A finite-element model of Antarctica: sensitivity test for meteorological mass-balance relationship. Journal of Glaciology 40 (134), 167-175.
- Fastook, J.L., Head, J.W., Marchant, D.R., Forget, F., 2008. Tropical mountain glaciers on Mars: altitude-dependence of ice accumulation, accumulation conditions, formation times, glacier dynamics, and implications for planetary spin-axis/ orbital history. Icarus 198, 305–317.
- Gair, H.S., 1967. Sheet 20-Mount Cook, Geological Map of New Zealand. Department of Scientific and Industrial Research, Wellington.
- Gersonde, R., et al., 2003. Last glacial sea surface temperatures and sea-ice extent in the Southern Ocean (Atlantic-Indian sector): a multiproxy approach. Paleoceanography 18 (3). http://dx.doi.org/10.1029/2002PA000809.
- Gersonde, R., Crosta, X., Abelmann, A., Armand, L., 2005. Sea-surface temperature and sea ice distribution of the Southern Ocean at the EPILOG Last Glacial Maximum - a circum-Antarctic view based on siliceous microfossil records. Quaternary Science Reviews 24 (7–9), 869–896.
- Ghisetti, F.C., Gorman, A.R., Sibson, R.H., 2007. Surface breakthrough of a basement fault by repeated seismic slip episodes: the Ostler Fault, South Island, New Zealand. Tectonics 26. http://dx.doi.org/10.1029/2007TC002146.
- Glen, J.W., 1955. The creep of polycrystalline ice. Proceedings of the Royal Society of London 228, 519-538
- Golledge, N.R., et al., 2012. Last Glacial Maximum climate in New Zealand inferred from a modelled Southern Alps icefield. Quaternary Science Reviews 46, 30-45.
- Gordon, A.L., 1981. Seasonality of Southern Ocean sea ice. Journal of Geophysical Research 86, 4193-4197.
- Gordon, A.L., 1991. Two stable modes of Southern Ocean winter stratification. In: Chu, P.C., Gascard, J.C. (Eds.), Deep Convection and Deep Water Formation in the Oceans. Elsevier Science Publishers B. V..
- Hays, J.D., Imbrie, J., Shackleton, N.J., 1976. Variations in the earth's orbit: pacemaker of the ice ages. Science 194 (4270), 1121-1132.
- Henderson, R.D., Thompson, S.M., 1999. Extreme rainfalls in the Southern Alps of New Zealand. Journal of Hydrology (NZ) 38, 309-330.
- Heusser, C.J., 1990. Chilotan piedmont glacier in the southern Andes during the last glacial maximum. Revista Geologíca de Chile 17, 3–18.
- Hijmans, R., Cameron, S.E., Parra, J.L., Jones, P.G., Jarvis, A., 2005. Very high resolution interpolated climate surfaces for global land areas. International Journal of Climatology 25, 1965-1978.
- Huybers, P., Denton, G., 2008. Antarctic temperature at orbital timescales controlled by local summer duration. Nature Geoscience 1 (11), 787-792.
- Huybers, P., 2009. Antarctica's orbital beat. Science 325 (5944), 1085–1086. Indermuhle, A., et al., 1999. Holocene carbon-cycle dynamics based on CO₂ trapped
- in ice at Taylor Dome, Antarctica. Nature 398 (6723), 121-126.
- Indermühle, A., Monnin, E., Stauffer, B., Stocker, T.F., Wahlen, M., 2000. Atmospheric CO₂ concentration from 60 to 20 kyr BP from the Taylor Dome ice core, Antarctica. Geophysical Research Letters 27 (5), 735–738.
- Johnson, J., Fastook, J.L., 2002. Northern Hemisphere glaciations and its sensitivity to basal melt water. Quaternary International 95–96, 65–74.
- Kaiser, J., Lamy, F., Hebbeln, D., 2005. A 70-kyr sea surface temperature record off southern Chile (Ocean Drilling Program Site 1233). Paleoceanography 20 (4), PA4009. http://dx.doi.org/10.1029/2005PA001146.
- Kaplan, M.R., et al., 2010. Glacier retreat in New Zealand during the Younger Dryas stadial. Nature 467, 194–197. Kaplan, M.R., et al., 2011. In-situ cosmogenic ¹⁰Be production rate at Lago Argentino,
- Patagonia: implications for late-glacial climate chronology. Earth and Planetary Science Letters 309, 21-32.
- Kawamura, K., et al., 2007. Northern Hemisphere forcing of climatic cycles in Antarctica over the past 360,000 years. Nature 448 (7156), 912-916.
- Keeling, R.F., Visbeck, M., 2011. On the linkage between Antarctic surface water stratification and global deep-water temperature. Journal of Climate 24, 3545-3557
- Kelly, M.A., 2003. The late Würmian Age in the western Swiss Alps last glacial maximum (LGM) ice-surface reconstruction and 10Be dating of late-glacial features. Ph.D. thesis. University of Bern, 105 pp.
- Laabs, B.J.C., Plummer, M.A., Mickelson, D.M., 2006. Climate during the last glacial maximum in the Wasatch and southern Uinta Mountains inferred from glacier modeling. Geomorphology 75, 300–317.
- Labeyrie, L., et al., 1996. Hydrographic changes of the Southern Ocean (southeast Indian sector) over the last 230 kyr. Paleoceanography 11 (1), 57-76.
- Lamont, G.N., Chinn, T.J.H., Fitzharris, B.B., 1999. Slopes of glacier ELAs in the Southern Alps of New Zealand in relation to atmospheric circulation patterns. Global and Planetary Change 22, 209–219. Lamy, F., et al., 2004. Antarctic timing of surface water changes off Chile and
- Patagonian ice sheet response. Science 304 (5679), 1959–1962.
- Lamy, F., et al., 2007. Modulation of the bipolar seesaw in the southeast pacific during Termination 1. Earth and Planetary Science Letters 259 (3–4), 400–413.

- Le Meur, E., Vincent, C., 2003. A two-dimensional shallow ice flow model of glacier de Saint Sorlin, France. Journal of Glaciology 49, 527–538.
- Le Meur, E., Gagliardini, O., Zwinger, T., Ruokolainen, J., 2004. Glacier flow modelling: a comparison of the shallow ice approximation and the full-Stokes solution. Comptes Rendus Physique 5 (7), 709–722.
 Le Meur, E., Gerbaux, M., Schäfer, M., Vincent, C., 2007. Disappearance of an alpine
- Le Meur, E., Gerbaux, M., Schäfer, M., Vincent, C., 2007. Disappearance of an alpine glacier over the 21st century simulated from modeling its future surface mass balance. Earth and Planetary Science Letters 261, 367–374.
- Lemieux-Dudon, B., et al., 2010. Consistent dating for Antarctic and Greenland ice cores. Quaternary Science Reviews 29 (1–2), 8–20.
 Leysinger Vieli, G., Gudmundsson, G.H., 2004. On estimating length fluctuations of
- Leysinger Vieli, G., Gudmundsson, G.H., 2004. On estimating length fluctuations of glaciers caused by changes in climatic forcing. Journal of Geophysical Research 109 (F1). http://dx.doi.org/10.1029/2003JF000027.
- Lifton, N., et al., 2005. Addressing solar modulation and long-term uncertainties in scaling secondary cosmic rays for in situ cosmogenic nuclide applications. Earth and Planetary Science Letters 239, 140–161.
- Lifton, N., Smart, B., Shea, M., 2008. Scaling time-integrated in situ cosmogenic nuclide production rates using a continuous geomagnetic model. Earth and Planetary Science Letters 268, 190–201.
- Lowell, T.V., Hayward, R.K., Denton, G.H., 1999. Role of climate oscillations in determining ice-margin position: hypothesis, examples, and implications. Geological Society of America Special Papers 337, 193–203.
- MARGO Project Members, 2009. Constraints on the magnitude and patterns of ocean cooling at the Last Glacial Maximum. Nature Geoscience 2, 127–132.
- McGlone, M.S., Moar, N.T., 1998. Dryland Holocene vegetation history, Central Otago and the Mackenzie Basin, South Island, New Zealand. New Zealand Journal of Botany 36, 91–111.
- Mercer, J.H., 1972. Chilean glacial chronology 20,000 to 11,000 carbon-14 years ago: some global comparisons. Science 176, 1118–1120.
- Mercer, J.H., 1984. Simultaneous climatic change in both hemispheres and similar bipolar warming: evidence and implications. In: Hansen, J.E., Takahashi, T. (Eds.), Climate Processes and Climate Sensitivity. Geophysical Monograph American Geophysical Union, Washington. D. C., pp. 307–313.
- Milankovitch, M., 1941. Kanon der Erdbestrahlung und seine Andwendung auf das Eiszeiten-problem. Royal Serbian Academy, Belgrade.
- Mix, A.C., Bard, E., Schneider, R., 2001. Environmental processes of the ice age: land, oceans, glaciers (EPILOG). Quaternary Science Reviews 20, 627–657.
- Monnin, E., et al., 2001. Atmospheric CO_2 concentrations over the last glacial termination. Science 291, 112–114.
- Newnham, R.M., Loewe, D.J., Giles, T., Alloway, B.V., 2007a. Vegetation and climate of Auckland, New Zealand, since ca. 32,000 cal. yr ago: support for an extended LGM. Journal of Quaternary Science 22 (5), 517–534.
- Newnham, R.M., Vandergoes, M.J., Hendy, C.H., Lowe, D.J., Preusser, F., 2007b.

 A terrestrial palynological record for the last two glacial cycles from southwestern New Zealand, Quaternary Science Reviews 26, 517–535.
- western New Zealand. Quaternary Science Reviews 26, 517–535.
 Nishiizumi, K., et al., 2007. Absolute calibration of ¹⁰Be AMS standards. Nuclear Instruments and Methods in Physics Research B 258, 403–413.
- Norton, D., 1985. A multivariate technique for estimating New Zealand temperature normals. Weather and Climate 5, 64–74.
- Oerlemans, J., 1997. Climate sensitivity of Franz Josef Glacier, New Zealand, as revealed by numerical modelling. Arctic and Alpine Research 29 (2), 233–239. Paterson, W.S.B., 1994. The Physics of Glaciers. Pergammon, Oxford.
- Pelejero, C., Calvo, E., Barrows, T.T., Logan, G.A., De Deckker, P., 2006. South Tasman Sea alkenone palaeothermometry over the last four glacial/interglacial cycles. Marine Geology 230, 73–86.
- Petit, J.R., et al., 1999. Climate and atmospheric history of the past 420,000 years from the Vostok ice core, Antarctica. Nature 399 (6735), 429–436.
- Porter, S.C., 1975. Equilibrium-line altitudes of Late Quaternary glaciers in the Southern Alps, New Zealand. Quaternary Research 5, 27–47.
- Purdie, H., et al., 2011. Interannual variability in net accumulation on Tasman Glacier and its relationship with climate. Global and Planetary Change. http://
- dx.doi.org/10.1016/j.gloplacha.2011.04.004.

 Putkonen, J., Swanson, T., 2003. Accuracy of cosmogenic ages for moraines.

 Quaternary Research 59, 255–261.
- Putnam, A.E., et al., 2010a. Glacier advance in southern middle latitudes during the Antarctic Cold Reversal. Nature Geoscience 3, 700–704.

- Putnam, A.E., et al., 2010b. In situ cosmogenic ¹⁰Be production-rate calibration from the Southern Alps, New Zealand. Quaternary Geochronology 5, 392–409.
- Refsnider, K.A., et al., 2008. Last glacial maximum climate inferences from cosmogenic dating and glacier modeling of the western Uinta ice field, Uinta Mountains, Utah. Quaternary Research 69, 130–144.
- Reimer, P.J., et al., 2009. INTCAL09 and MARINE09 radiocarbon age calibration curves, 0–50,000 years cal BP. Radiocarbon 51 (4), 1111–1150.
- Robinson, R.S., Mix, A., Martinez, P., 2007. Southern Ocean control on the extent of denitrification in the southeast Pacific over the last 70 ka. Quaternary Science Reviews 26 (1–2), 201–212.
- Roe, G., 2006. In defense of Milankovitch. Geophysical Research Letters 33 (L24703). http://dx.doi.org/10.1029/2006GL027817.
- Sandiford, A., Newnham, R.M., Alloway, B.V., Ogden, J., 2003. A 28 000–7600 yr BP pollen record of vegetation and climate change from the Pukaki Crater, northern New Zealand. Palaeogeography Palaeoclimatology Palaeoecology 201, 235–247.
- Schaefer, J.M., et al., 2006. Near-synchronous interhemispheric termination of the last glacial maximum in mid-latitudes. Science 312 (5779), 1510–1513.
- Schaefer, J.M., et al., 2009. High-frequency Holocene glacier fluctuations in New Zealand differ from the northern signature. Science 324, 622–625.
- Schäfer, M., Gagliardini, O., Pattyn, F., Le Meur, E., 2008. Applicability of the shallow ice approximation inferred from model inter-comparison using various glacier geometries. Cryosphere Discussions 2 (4), 557–599.
- Shemesh, A., et al., 2002. Sequence of events during the last deglaciation in Southern Ocean sediments and Antarctic ice cores. Paleoceanography 17 (4). http://dx.doi.org/10.1029/2000PA000599.
- Sigman, D.M., Haug, G.H. (Eds.), 2003. The Biological Pump in the Past. Treatise on Geochemistry, vol. 6. Elsevier Pergamon.
- Sigman, D.M., Jaccard, S.L., Haug, G.H., 2004. Polar ocean stratification in a cold climate. Nature 428 (6978), 59–63.
- Sigman, D.M., de Boer, A.M., Haug, G.H., 2007. Antarctic stratification, atmospheric water vapor, and Heinrich Events: a hypothesis for Late Pleistocene deglaciations. In: Schmittner, A., Chiang, J.C.H., Hemming, S.R. (Eds.), Ocean Circulation: Mechanisms and Impacts. Geophysical Monograph Series, vol. 173. American Geophysical Union, Washington, pp. 335—349.
- Sigman, D.M., Hain, M.P., Haug, G.H., 2010. The polar ocean and glacial cycles in atmospheric ${\rm CO_2}$ concentration. Nature 466, 47–55.
- Sikes, E.L., et al., 2009. Southern Ocean seasonal temperature and Subtropical Front movement on the South Tasman Rise in the late Quaternary. Paleoceanography 24 PA2201
- Staiger, J., et al., 2007. Atmospheric scaling of cosmogenic nuclide production: climate effect. Journal of Geophysical Research 112. http://dx.doi.org/10.1029/ 2005IB003811.
- Stone, J.O., 2000. Air pressure and cosmogenic isotope production. Journal of Geophysical Research 105, 23753—23759.
- Strelin, J.A., Denton, G.H., Vandergoes, M.J., Ninnemann, U.S., Putnam, A.E., 2011. Radio-carbon chronology of the late-glacial Puerto Bandera moraines, Southern Patagonian Icefield, Argentina. Quaternary Science Reviews 30 (19–20), 2551–2569.
- Sugden, D.E., John, B.S., 1976. Glaciers and Landscape: a Geomorphological Approach. Edward Arnold, London.
- Suggate, R.P., 1990. Late Pliocene and Quaternary glaciations of New Zealand. Quaternary Science Reviews 9, 175–197.
- Toggweiler, J.R., Russell, J.L., Carson, S.R., 2006. Midlatitude westerlies, atmospheric CO₂, and climate change during the ice ages. Paleoceanography 21 (2), PA2005.
- Toggweiler, J.R., 2008. Origin of the 100,000-year timescale in Antarctic temperatures and atmospheric CO₂. Paleoceanography 23 (2), PA2211. http://dx.doi.org/ 10.1029/2006PA001405.
- Toggweiler, J.R., 2009. Shifting westerlies. Science 323 (5920), 1434–1435.
- Vandergoes, M.J., et al., 2005. Regional insolation forcing of late Quaternary climate change in the Southern Hemisphere. Nature 436, 242–245.
- Ward, G.K., Wilson, S.R., 1978. Procedures for comparing and combining radiocarbon age determinations: a critique. Archaeometry 20, 19–31. Weertman, J., 1964. The theory of glacier sliding. Journal of Glaciology 5 (39), 287–303.
- Weertman, J., 1964. The theory of glacier sliding. Journal of Glaciology 5 (39), 287–303. Whittaker, T.E., Hendy, C.H., Hellstrom, J.C., 2011. Abrupt millennial-scale changes in intensity of Southern Hemisphere westerly winds during marine isotope stages 2–4. Geology 39 (5), 455–458.